



## WEAR RESISTANCE OF LAYERS HARD FACED BY THE HIGH-ALLOYED FILLER METAL

Dušan Arsić<sup>1</sup>, Vukić Lazić<sup>1</sup>, Ružica Radoslava Nikolić<sup>1,2,\*</sup>, Milan Mutavdžić<sup>3</sup>, Srbislav Aleksandrović<sup>1</sup>, Milan Djordjević<sup>1</sup>

<sup>1</sup>Faculty of Engineering, University of Kragujevac, Sestre Janjić 6, 34000 Kragujevac, Serbia

<sup>2</sup>Research Center, University of Žilina, Univerzitná 1, 010 26 Žilina, Slovak Republic

<sup>3</sup>High Technical School, November nn, 38218 Leposavić, Serbia

\*correspondingauthor: e-mail: ruzicarnikolic@yahoo.com

### Resume

The objective of this work was to determine the wear resistance of layers hard faced by the high-alloyed filler metal, with or without the austenite inter-layer, on parts that operate at different sliding speeds in conditions without lubrication. The samples were hard faced with the filler metal E 10-UM-60-C with high content of C, Cr and W. Used filler metal belongs into a group of alloys aimed for reparatory hard facing of parts damaged by abrasive and erosive wear and it is characterized by high hardness and wear resistance. In experiments, the sliding speed and the normal loading were varied and the wear scar was monitored, based on which the volume of the worn material was calculated analytically. The contact duration time was monitored over the sliding path of 300 mm. The most intensive wear was established for the loading force of 100 N and the sliding speed of 1 m.s<sup>-1</sup>, though the significant wear was also noticed in conditions of the small loading and speed of 0.25 m.s<sup>-1</sup>, which was even greater than at larger speeds.

### Article info

#### Article history:

Received 02 February 2016

Accepted 22 July 2016

Online 22 October 2016

#### Keywords:

Hard facing;

Filler metal;

Abrasive wear;

Wear resistance;

Sliding speed.

Available online: <http://fstroj.uniza.sk/journal-mi/PDF/2016/12-2016.pdf>

ISSN 1335-0803 (print version)

ISSN 1338-6174 (online version)

### 1. Introduction

Large number of machine parts and devices, especially in construction industry are exposed, on a daily basis, to rigorous exploitation conditions when the working parts of machines and devices are in the constant contact with hard and brittle abrasive materials. Due to their high hardness, such materials affect the working life of parts causing its shortening. Frequently, the working parts lose their original designed geometry, while the fracture of parts is frequent, as well. To prevent that and to extend the working life of parts, like the stone crusher's teeth [1], loading excavator bucket's teeth [2] knives of the terrain leveling grader board [3] and others, there is a tendency to manufacture them from the high quality and more adequate materials. However, even thus manufactured parts are worn relatively quickly, so the necessity

for their replacement or repair occurs. Considering that waiting for purchase of the new part could last quite a long time, what is usually accompanied with high costs, the alternative is repair by hard facing of the damaged parts.

The repair by hard facing can create significant savings [4, 5], while simultaneously the working surfaces, which are more wear resistant than those on the original new parts are, are obtained. This subject was investigated by authors of paper [6 - 8] and [9 - 19] and in those papers the previously stated observations were confirmed. Thus, the objective of this work was to establish the possibility for extending the working life of the machine parts by hard facing the damaged surfaces with use of the adequate filler metal and to determine the influence of the sliding speed in the tribological

tests on the hard faced layers' characteristics.

The previous investigations of certain materials with similar properties to those used in this research have established that the loss of materials' mass increases with increase of the loading, which can be taken for granted, and with increase of the sliding speed, which was to be confirmed with experiments performed within this investigation. Authors of [20] have investigated the grey cast iron with high carbon content, while in [21] authors were dealing with analysis of the Fe-Cr-B alloy aimed for hard facing, which has the similar content as the filler metal used in this paper. The applied sliding speeds were of 0.25, 0.5 and 1 m.s<sup>-1</sup>, while the applied loads were of 50, 75 and 100 N and the purpose was to determine the wear resistance of the analyzed filler metal.

## 2. Samples preparation and plan of experiments

One of the most difficult steps in prescribing the hard facing technology is selection of the filler metal (FM). It should be selected in such a manner that it possesses high hardness and wear resistance and simultaneously to have the favorable weldability. The filler metal, analyzed in this paper, is the high-alloyed steel with high content of carbon, chromium and tungsten, marked as E 10-UM-60-C (DIN standard 8555). Such a chemical composition ensures the high hardness and wear resistance of this filler metal, which is prescribed by the manufacturer for parts that work in such conditions.

Prior to hard facing, the base metal (BM)

is usually preheated to improve its weldability; in this case, the preheating temperature was defined as 250 °C. However, in some cases, due to some restrictions, like the BM chemical composition or lack of the preheating equipment in the field, the preheating cannot be done, so it is usually replaced by deposition of the interlayer of the austenitic FM. The applied BM is the stainless steel marked as E 18 8 Mn B 20+ (DIN standard 8555).

The chemical composition of the base metal (BM) and the filler metals (FM#1 and FM#2) is given in Table 1.

The hard facing parameters were current 125 A and voltage 25 V, with the welding speed of 1.9 mm.s<sup>-1</sup>. The plate of BM of 10 mm thickness was hard faced with such parameters, with three layers, so that adequate thickness is obtained to enable cutting out the samples for tribological investigations. For samples with the interlayer, the first layer was deposited by the FM of the stainless steel (#2), while the other two layers were deposited by the FM for hard facing (#1). Preparation – cutting out – of the samples for tribological investigations was done according to Fig. 1a, while the samples for measurement of hardness and analysis of microstructure were prepared according to Fig. 1b. In addition, besides samples (blocks) prepared from the hard faced layers, the blocks of the same dimensions were prepared from the base metal.

Tribological test assumed subjecting the samples, cut-out from the hard faced layers and the BM, to the wear test on the tribometer with the block-on-disc contact (Fig. 2).

*Table 1*  
*Chemical composition of base metal and filler metals.*

Steel/Electrodes	Alloying elements %										Hardness HRC
	C	Si	Mn	P	S	Cr	Mo	W	Ni	Al	
<b>BM S355J0</b>	0.2	0.55	1.4	0.045	0.045	0.3	0.08	-	0.3	0.02	≈ 28
<b>FM1 E 10-UM-60-C</b>	4.0	-	-	-	-	26	-	4.0	-	-	57 - 62
<b>FM2 E 18 8 Mn B 20+</b>	0.12	0.8	7.0	-	-	19	-	-	9.0	-	-

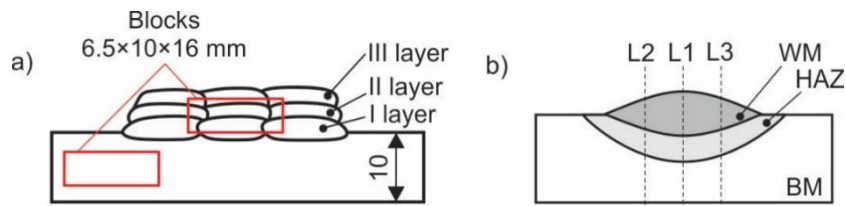
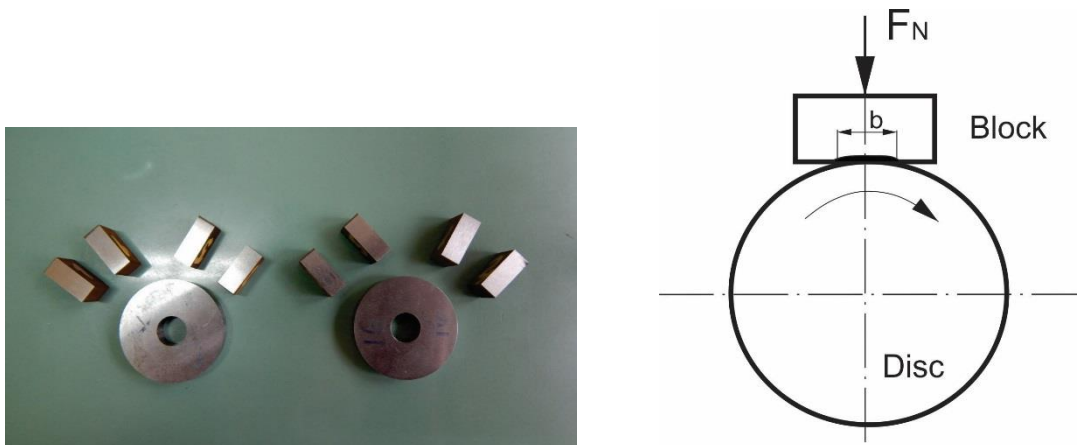


Fig. 1. Layer deposition and block for tribological testing (a) and metallographic sample (b); L1, L2 and L3 denote the directions of hardness measurements.  
(full colour version available online)



a) prepared blocks and discs  
(full colour version available online)  
b) block-on-disc contact scheme  
Fig. 2. Prepared blocks and discs and block-on-disc contact scheme.  
(full colour version available online)

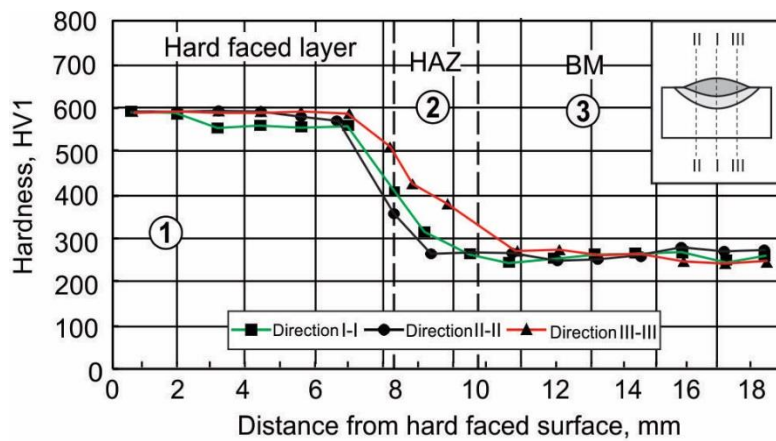


Fig. 3. Hardness distribution (diagram above) and the microstructures of the WM (1), HAZ (2) and BM (3) pictures (below).  
(full colour version available online)

### 3. Results and discussion

#### 3.1 Hardness measurement and microstructure analysis

Hardness was measured on samples prepared according to Fig. 1 and it was used to form curves of the hardness distribution in the three characteristic parallel directions (L1, L2 and L3). Besides that, the characteristic microstructures were recorded in the three zones of the hard faced layer – in the weld metal (WM), heat affected zone (HAZ) and in the base metal (BM). Etching of samples was done in two phases. In the first phase, samples were etched by the 3 % Nital solution (in denatured alcohol) and after that, only the zones of the BM and the HAZ were visible. Then, in the second phase, the samples were etched by the 4 % Vilelle solution. This solution is very aggressive and it can provide good quality etching of the highly alloyed hard faced layers. Results of the hardness measurements and the microstructures of the individual hard faced layer's zones are presented in Fig. 3.

From the graph in Fig. 3 one can see that the hard faced layer hardness is about 600 HV1, what corresponds to the data provided by the manufacturer. It can also be noticed that hardness was maintained over the whole cross section of the hard faced layer (average thickness of about 7 mm), after which it drops within the HAZ and the BM.

The BM microstructure was estimated as ferritic-perlite, while the microstructure of the FM was ledeburite–cast structure with excreted carbides. They possess the high hardness what should ensure the improved wear resistance.

#### 3.2 Tribological test

The wear resistance was determined by measurements of the wear scar and then it was used to calculate the volume of the worn material. The wear scar width was recorded by the optical microscope with magnification 50×. The parameter for the contact duration was the path of 300 mm, which means that

the contact time was different for different sliding speeds. The friction coefficient was also recorded, besides the wear scar width, during the sliding process under different conditions. The tests were done without application of lubricants. Obtained results are presented as graphs in Fig. 4 and in Table 2, while the macroscopic and microscopic appearances of the damaged surface of some blocks are shown in Fig. 5. The worn material volume was calculated based on the measured length and width of the wear scar. In the computer program the volume of the block mass, "eaten" by the disc is then calculated.

Obtained results show that the hard faced layers possess significantly higher wear resistance than the base metal, as it was expected. The curves in Fig. 4 show increase of the worn material mass with increase of the sliding speed and the normal loading, all the way up to reaching the highest degree of wear at maximum load of 100 N and at the highest speed of 1 m.s<sup>-1</sup> (Fig. 4c), what was also confirmed by some other investigations [17, 20].

However, it is interesting that almost the same results were obtained for the case of the applied force of 75 N at sliding speeds of 0.5 and 1 m.s<sup>-1</sup> (Fig. 4b). This means that increase of speed from 0.5 to 1 m/s, at that load does not have any influence. In addition, results show that at the loading force of 50 N, the optimal sliding speed 0.5 m.s<sup>-1</sup>, since the wear is the least (Fig. 4a). Results have also shown that there is no big difference in wear behavior between samples with and without austenitic interlayer (Table 2 – sample #3 has even somewhat higher resistance), what means that the interlayer can be used whenever it is necessary and that would not influence the wear resistance of the hard faced layers.

Photos in Fig. 5 show the characteristic damages of the tested materials surfaces. The characteristic phenomena in the initial stadium of wear are appearances of crevices and wear scars. However, after a certain distance,

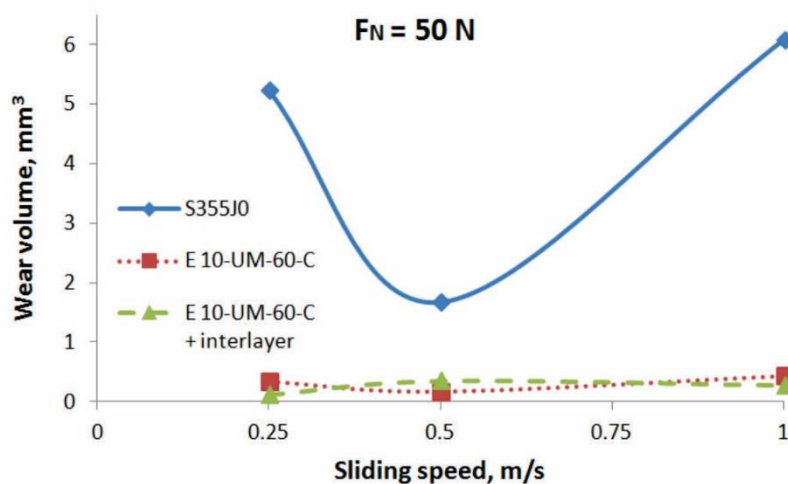
at the crack sites material particles started to detach from the sample's surface, usually due to adhesion to disc material [20]. Those particles can later also act as the abrasive and induce further damages. The shown damages are in accordance with the results obtained for steel

S355J0 [22], verifying the fact that it possesses poor wear resistance. On the other hand, the hard faced sample exhibits the higher wear resistance and its wear scar is significantly smaller and there is no appearance of spots of the material detachments from individual zones.

Table 2

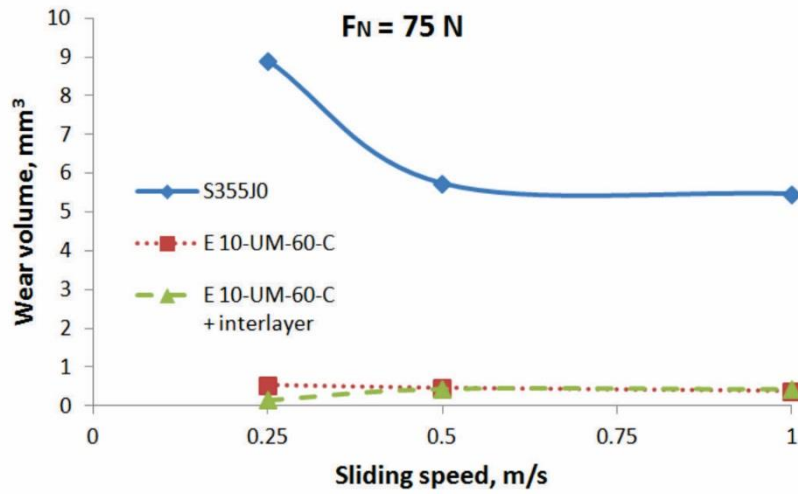
Obtained values of the wear scar width and volume of the worn material for the BM and FM.

		Worn material volume, mm <sup>3</sup>			Wear scar width, mm		
SAMPLE #1		Base metal - S355J0			Base metal - S355J0		
Sliding speed, m.s <sup>-1</sup>	Load, N			Load, N			
	50	75	100	50	75	100	
0.25	5.23779	8.89852	9.36935	4.97	5.91	6.01	
0.5	1.67035	5.73512	9.95678	3.41	5.12	6.13	
1	6.08405	5.46604	17.9884	5.22	5.04	7.42	
SAMPLE #2		Filler metal - E 10-UM-60-C			Filler metal - E 10-UM-60-C		
Sliding speed, m.s <sup>-1</sup>	Load, N			Load, N			
	50	75	100	50	75	100	
0.25	0.33811	0.54007	0.61469	2.007	2.345	2.448	
0.5	0.16379	0.47241	0.63226	1.577	2.243	2.471	
1	0.43419	0.39641	1.24646	2.181	2.116	3.095	
SAMPLE #3		Filler metal - E 10-UM-60-C + austenite interlayer			Filler metal - E 10-UM-60-C + austenite interlayer		
Sliding speed, m.s <sup>-1</sup>	Load, N			Load, N			
	50	75	100	50	75	100	
0.25	0.118771	0.156112	0.323632	1.417	1.552	1.978	
0.5	0.350939	0.426453	0.469876	2.032	2.168	2.239	
1	0.279109	0.421149	0.556171	1.883	2.159	2.368	

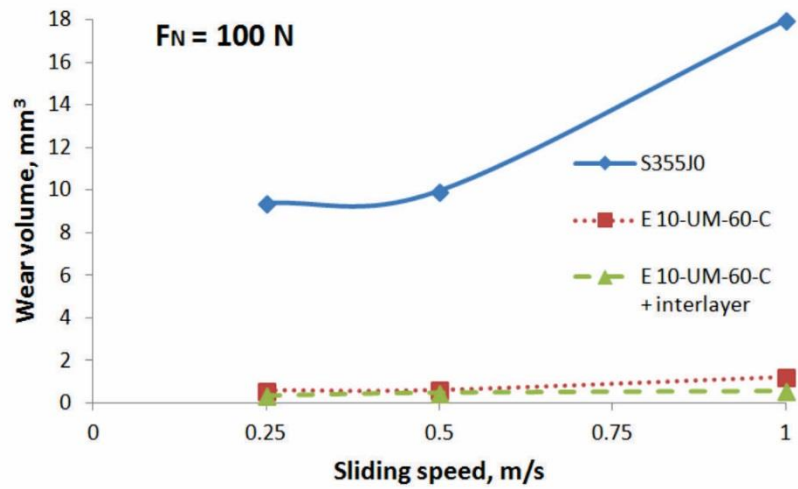


a) 50 N

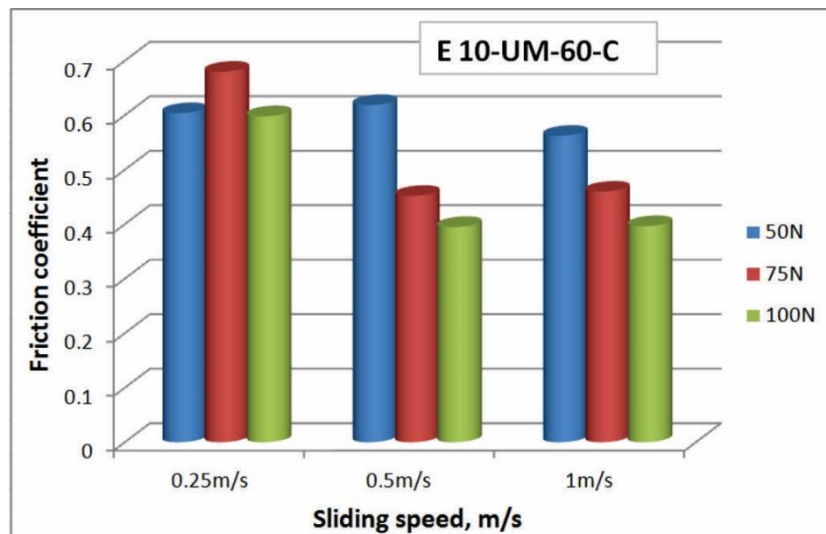
Fig. 4. Worn material volume at different loads and histogram of the friction coefficient average values for all the loads and sliding speeds.



b) 75 N



c) 100 N



d) histogram of the friction coefficient average values for all the loads and sliding speeds  
 Continuing of Fig. 4. Worn material volume at different loads and histogram of the friction coefficient average values for all the loads and sliding speeds.  
 (full colour version available online)

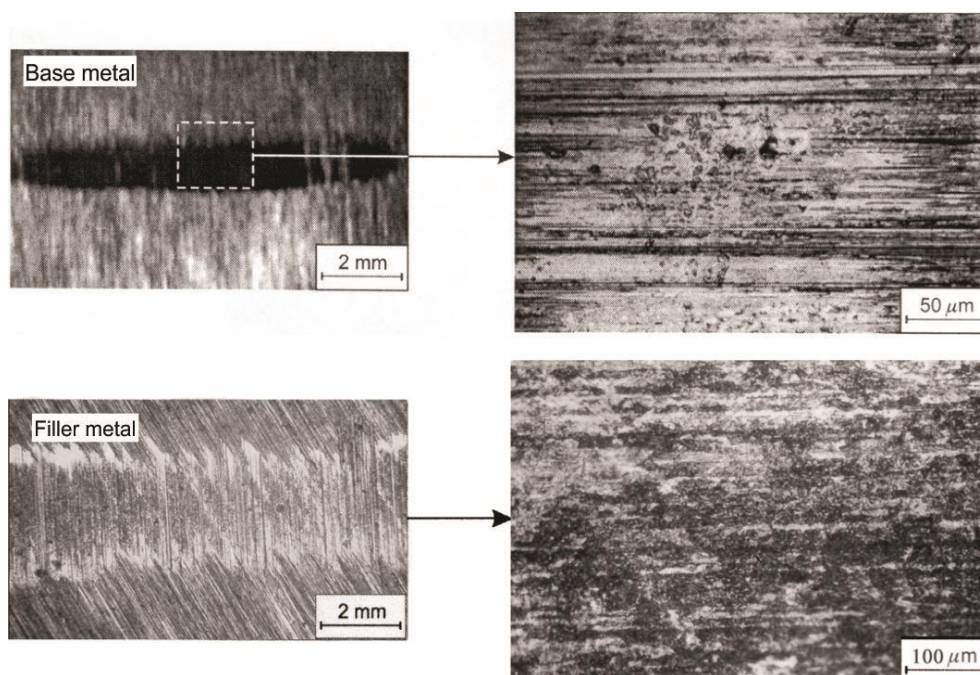


Fig. 5. Macroscopic (left) and microscopic (right) appearances of the damaged blocks of the hard faced layers.

#### 4. Conclusions

An analysis of the sliding speed influence in tribological tests, on the wear resistance of the base metal and the hard faced layers of the test samples is presented in this paper. Measurements of hardness and analysis of microstructure have shown that the base metal and the filler metal differ significantly and that the filler metal is characterized by the cast structure with the excreted carbides, what predetermines it as a material favorable for application in hard facing. The highest hardness was obtained in the surface welded hard faced layers (FM) and then it was gradually decreasing down to the base metal hardness.

Besides varying the sliding speed and absence of lubrication, the investigation also included varying of the normal loading. Results have shown that the tested FM possesses high wear resistance. On the other hand, the sample hard faced with the same FM, but with austenitic interlayer, have exhibited slightly better wear resistance, what points to recommendation to apply the interlayer whenever the preheating cannot be executed.

Influence of the sliding speed is obvious, since it is expected that the wear would increase with increasing sliding speed. It was maximal at sliding speed of  $1 \text{ m}\cdot\text{s}^{-1}$  and load of 100 N, for both the BM and the FM. However, there were certain cases of deviation from the usual behavior, at loads of 50 and 75 N, when the wear was the more intensive at the smallest sliding speed of  $0.25 \text{ m}\cdot\text{s}^{-1}$ , then it decreased and later increased again (Fig. 3a) or when it settled at lower values (Fig. 3b).

The technology presented in this paper was later applied on real parts – the blades for asphalt mixing were hard faced and then used in exploitation.

#### Acknowledgements

*This research was partially financially supported by European regional development fund and Slovak state budget by the project "Research Centre of the University of Žilina" – ITMS 26220220183 and by the Ministry of Education, Science and Technological Development of Republic of Serbia through grants: ON174004, TR32036, TR35024 and TR33015.*

## Note

The shorter version of this research was presented at the SEMDOK 2016 International Seminar, 27. – 29. January, 2016, Terchova, Slovakia, reference [22].

## References

- [1] S. Jozić, D. Bajić, A. Stoić: *Metalurgija – Metallurgy* 54(2) (2015) 343-346.
- [2] Z. Lazarević, I. Arandelović, S. Kirin: *Structural Integrity and Life* 15(3) (2015) 143-146.
- [3] B. Nedeljković, M. Babić, M. Mutavdžić, N. Ratković, S. Aleksandrović, R. Nikolić, V. Lazić: *J. Balkan Tribol. Assoc.* 16(1) (2008) 46-57.
- [4] V. Lazić, D. Arsić, M. Mutavdžić, R. Nikolić, B. Hadzima, N. Ratković: In *Proc. Of 43. International Conference Zvaranie 2015, Tatranská Lomnica, Slovakia 2015*, pp. 15-27.
- [5] V. Lazić, R. Čukić, S. Aleksandrović, D. Milosavljević, D. Arsić, B. Nedeljković, M. Djordjević: *Tribology in Industry* 36(3) (2015) 287-292.
- [6] D. Arsić, V. Lazić, I. Samardžić, R. Nikolić, S. Aleksandrović, M. Djordjević, B. Hadzima: *Tehnički Vjesnik – Technical Gazette* 22(5) (2015) 1353-1358.
- [7] V. Lazić, M. Jovanović, D. Milosavljević, M. Mutavdžić, R. Čukić: *Tribology in Industry* 30(1&2) (2008) 3-10.
- [8] V. Lazić, A. Sedmak, S. Aleksandrović, D. Milosavljević, R. Čukić, V. Grabulov: *Tehnički Vjesnik – Technical Gazette* 16(4) (2009) 107-113.
- [9] V. Lazić, M. Mutavdžić, D. Milosavljević, S. Aleksandrović, B. Nedeljković, P. Marinković, R. Čukić: *Tribology in industry* 33(1) (2011) 18-27.
- [10] S. Marković, Lj. Milović, A. Marinković, T. Lazović: *Structural Integrity and Life* 11(2) (2011) 127-130.
- [11] J. Truhan, R. Menon, F. LeClaire, J. Wallin, J. Qu, P. Blau: *Wear* 263 (2007) 234-239.
- [12] A. S. Kang, G. S. Cheema, S. Singla: *Procedia Engineering* 97 (2014) 1442-1451.
- [13] D. Liu, R. Liu, Y. Wei, Y. Ma, K. Zhu: *Applied Surface Science* 271 (2013) 253-259.
- [14] J. Laurila, A. Milanti, J. Nurminen, M. Kallio, P. Vuoristo: *Wear* 307 (2013) 142-149.
- [15] Chi-Ming Lin, Chia-Ming Chang, Jie-Hao Chen, Weite Wu: *J. of Alloys and Compounds* 498 (2010) 30-36.
- [16] W. Żurowski: *Eksploatacja i Niezawodność – Maintenance and Reliability* 14(1) (2012) 19-23.
- [17] C. Chang, Y. Chen, W. Wu: *Tribology International* 43(5-6) (2010) 929-934.
- [18] A. Zavos, P. Nikolakopoulos: *FME Transactions* 43(3) (2015) 191-197.
- [19] M. Hawryluk, M. Marciniak, G. Misiun: *Eksploatacja I Niezawodność – Maintenance and Reliability* 16(4) (2014) 600-607.
- [20] B. K. Prasad: *Tribology – Materials, Surfaces & Interfaces* 2(3) (2008) 128-138.
- [21] G. Cui, J. Wei, G. Wu: *Industrial Lubrication and Tribology* 67(4) (2015) 336-343.
- [22] D. Arsić, V. Lazić, R. R. Nikolić, S. Aleksandrović, M. Djordjević: In *Proc. of Abstracts of 21<sup>st</sup> International Seminar "SEMDOK 2016"*, Terchova, Slovakia 2016, 8.



# EXPERIMENTAL AND NUMERICAL INVESTIGATION OF A SIMPLIFIED EXHAUST MODEL

Balázs Vehovszky<sup>1,\*</sup>, Tamás Jakubík<sup>1</sup>, Martin Schuster<sup>2</sup>

<sup>1</sup> Department of Whole Vehicle Engineering, Audi Hungaria Faculty of Vehicle Engineering, Széchenyi István University, Egyetem tér 1, 9026 Győr, Hungary

<sup>2</sup> Whole Vehicle Development, Audi Hungaria Motor Kft., Kardán utca 1, 9026 Győr, Hungary

\*corresponding author: e-mail: [vehovszky.balazs@sze.hu](mailto:vehovszky.balazs@sze.hu)

## Resume

A simplified experimental equipment was built to investigate heat radiation and free convection around hot exhaust pipe. Temperatures were measured on the surface of the pipe as like as on heat insulating and -reflecting aluminum shield. Special care was taken to the temperature measuring method: result proved that inappropriate fixing of measuring thermocouples lead to an error of up to 30 % in the temperature-increase values. A detailed 1D numerical model was set up and parametrized so as to the calculation results can be fitted to measured temperature values. In this way thermal properties of the surfaces – as emissivities, absorption coefficients and convective heat transfer coefficients – were determined for temperature sweeps and stationary state cases. The used methods are to be further improved for real automotive parts and higher temperatures.

## Article info

### Article history:

Received 06 July 2016

Accepted 08 August 2016

Online 22 October 2016

### Keywords:

Thermal characterization;  
Exhaust system;  
Temperature measurement;  
Parameter fitting;  
Numerical model

Available online: <http://fstroj.uniza.sk/journal-mi/PDF/2016/13-2016.pdf>

ISSN 1335-0803 (print version)  
ISSN 1338-6174 (online version)

## 1. Introduction

Large Heat flow around vehicle exhaust system is of great importance as regards heat insulating and other elements nearby hot parts. Experimental results as like as numerical simulations are commonly used to handle thermal effects [1, 2]; however, the results of these examinations are not always consistent. Inaccurate radiation settings in the numerical model and erroneous estimation of free convection are among the most usual reasons of this delusion [3].

Regarding real in-vehicle operation, the overheating of exhaust heat reflecting shield and nearby elements during heavy duty operations can be the consequence of an improper heat design. The risk of this malfunction is extremely increased when the combination of high exhaust temperature (due to e.g. high engine performance)

with low forced flow (i.e. low vehicle speed) occurs. Such conditions can come up for example when the car stops immediately after a forced highway run, or during pulling heavy load uphill [4]. Dirt on the heat reflecting elements or extreme ambient conditions (e.g. hot black asphalt) further increases the chance of exhaust system overheating.

To handle this issue, well-harmonized experiments and numerical simulations should be executed. During our work we targeted the investigation of an in-between area: a simple model measurement, which could be effectively parametrized for real conditions and accurately simulated numerically. The two most unsettled processes: the heat radiation and the free convection are in the focus of our research, which were examined via experimental and numerical methods.

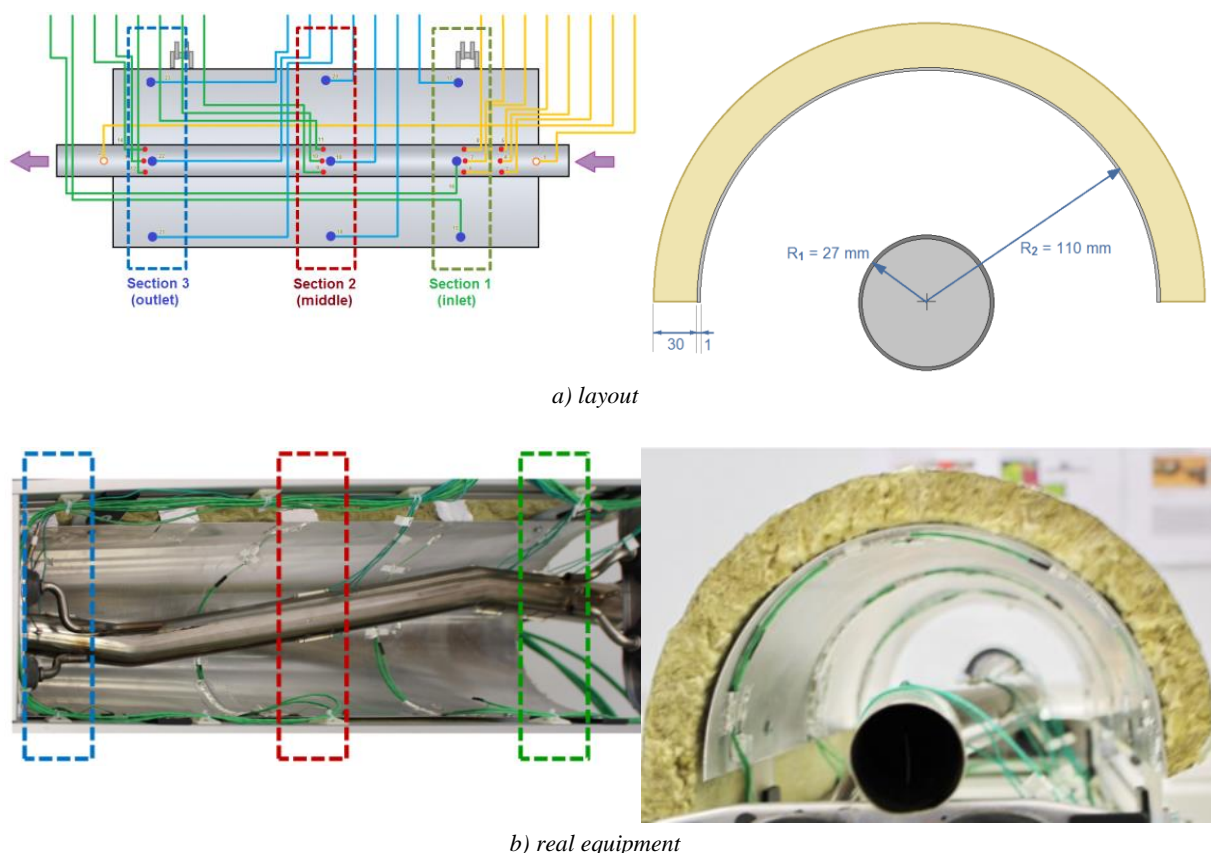
## 2. Experiments

A simplified exhaust tube – heat reflecting shield setup was designed and built aiming the effective modelling of heat transfer processes. The equipment consists of a part of an exhaust tube (stainless steel, OD Ø54 mm) with its fittings, a hot air supply (Steinel 3483 heat gun, up to 650°C air temperature), a half cylinder-shape aluminum heatshield (Ø220 mm) with 30 mm rock wool outer insulation and 23 temperature measurement points (K-type thermocouples, 4×3 on the tube – marked with red dots, 3×3 on the heatshield – marked with blue dots and 2 inside the tube for measuring heating air temperature – marked with hollow orange dots, see Fig. 1). Three main sections along the tube were defined: the inflat side has the highest

temperature while the outlet has the lowest.

During the design of the apparatus special care was taken to:

- Hot air inlet to exclude ambient temperature suck (resulting cooler tube);
- Fixing of hot elements to minimize heat transfer via conduction (using heat resistant rubber and silicone fixtures);
- Fixing the thermocouples:
  - Air temperature was measured with coaxial, hermetically insulated ones
  - Tube surface temperature was measured with spot-welded thermocouples
  - Thermocouples on the aluminum heatshield (inner side) were fixed by aluminum adhesive tape – the effect of fixing method was also investigated.



b) real equipment  
 Fig. 1. The measurement scheme.  
 (full colour version available online)

Basic measurement course was started at ambient temperature for all parts of the apparatus. During continuous registration of the temperatures the heat gun was switched on and the tube started to heat up; meanwhile the heatshield warms up too due to heat radiation and convection. After around 1 hour the temperature of the system becomes stationary resulting a  $\Delta T_G$ ,  $\Delta T_T$  and  $\Delta T_S$  temperature excess compared to ambient temperature for the gas, the tube and the heatshield, respectively (see Fig. 2).

For being able to investigate the effect of thermal convection and heat radiation separately, the apparatus was designed for operation in normal and upside-down (inverted) position too. Latter one excludes heat convection from the exhaust tube  $\rightarrow$  heatshield heat transfer path (see Fig. 3).

The effectiveness of heat flow (thermal convection) elimination during inverted setup measurement was proven by measuring the temperature of the heatshield surface and the air temperature just above the heatshield (see Fig. 4). If considerable heat flow occurs between the tube and the heatshield, the air temperature would be higher than that of the surface (the air would heat the shield). In contrast, air temperature was equal

or slightly below the shield surface temperature, which proves that no significant heat flow via air occurs between the tube and the heatshield (practically, the shield warms up the air above itself).

Taking into account the above considerations, one can conclude that in the reversed position the only heat transfer path from the heated tube to the heatshield is thermal radiation. Thus, at this setup mode the clear radiation properties can be examined concerning the heat input of the heatshield. Furthermore, comparing the results of normal and inverted position measurements, the impact of free thermal convection on the warming of heatshield can be calculated.

Aiming the investigation of different surface qualities, two modifications of the aluminum heatshield inner side were tested beside the base (as-rolled aluminum sheet) surface (see Fig. 5):

- Modification of roughness: polished and roughened with sandpaper (P120 grit);
- Modification of color: coated with black (Kontakt Chemie Graphit 33) and white (MR Chemie MR 70 developer white) sprayed layer;

The surface color modification of exhaust tube was also investigated.

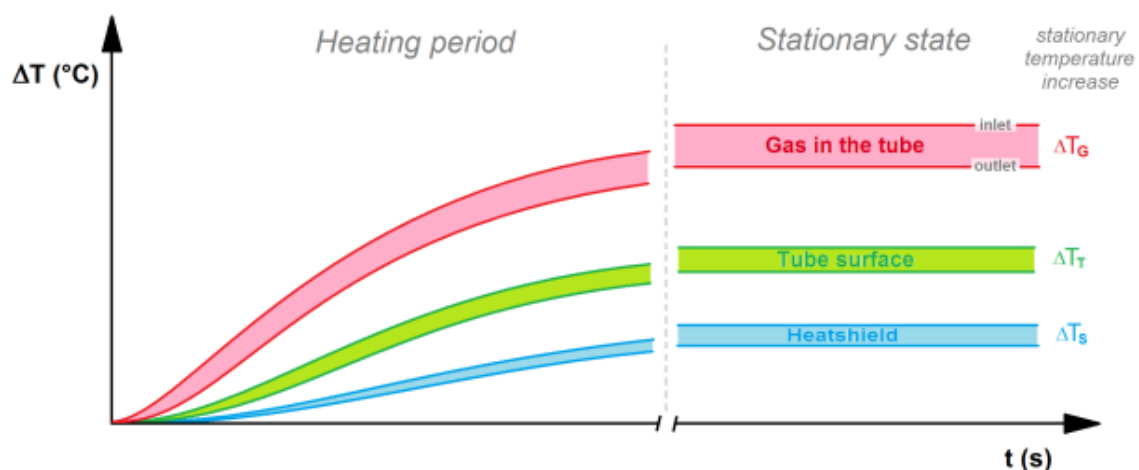


Fig. 2. The characteristic temperature increase of the gas ( $\Delta T_G$ ), the tube ( $\Delta T_T$ ) and the heatshield ( $\Delta T_S$ ) during heating up and in stationary state.  
(full colour version available online)

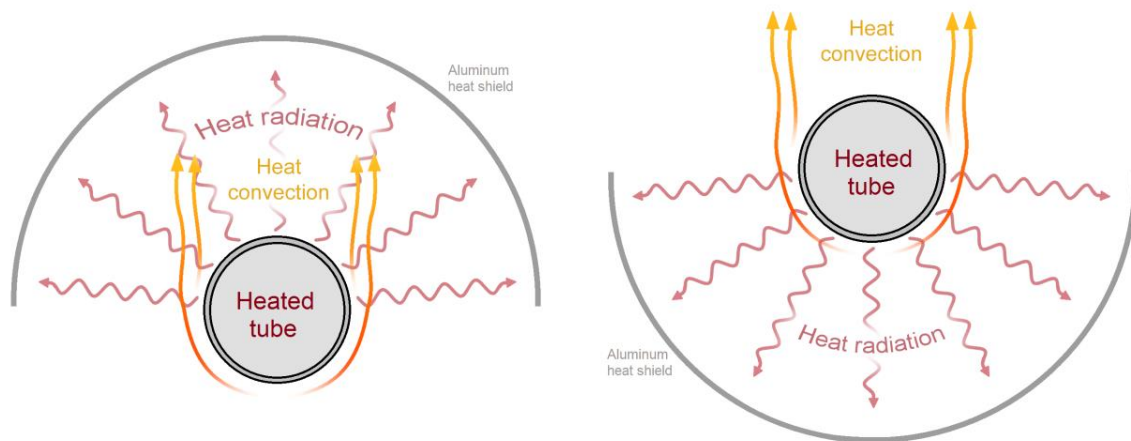


Fig. 3. Heat transfer from tube to heatshield at normal (left) and inverted (upside-down, right) position. (full colour version available online)

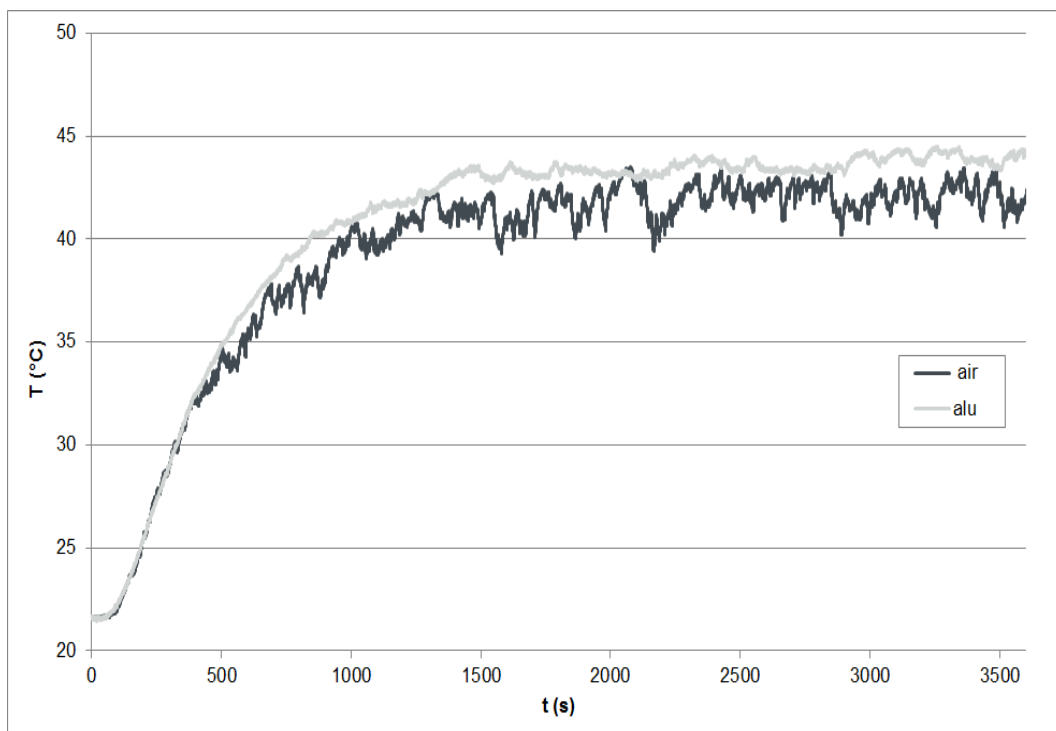
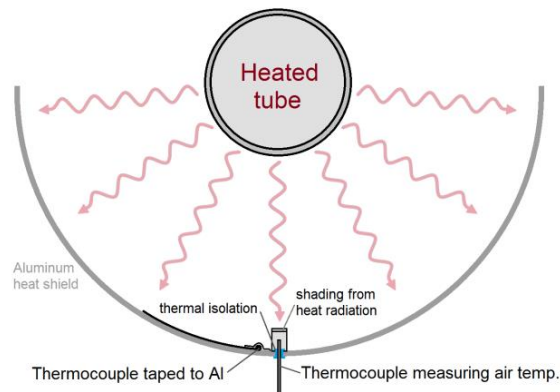


Fig. 4. Temperature measurement at inverted position proved the absence of heat flow from the tube. (full colour version available online)

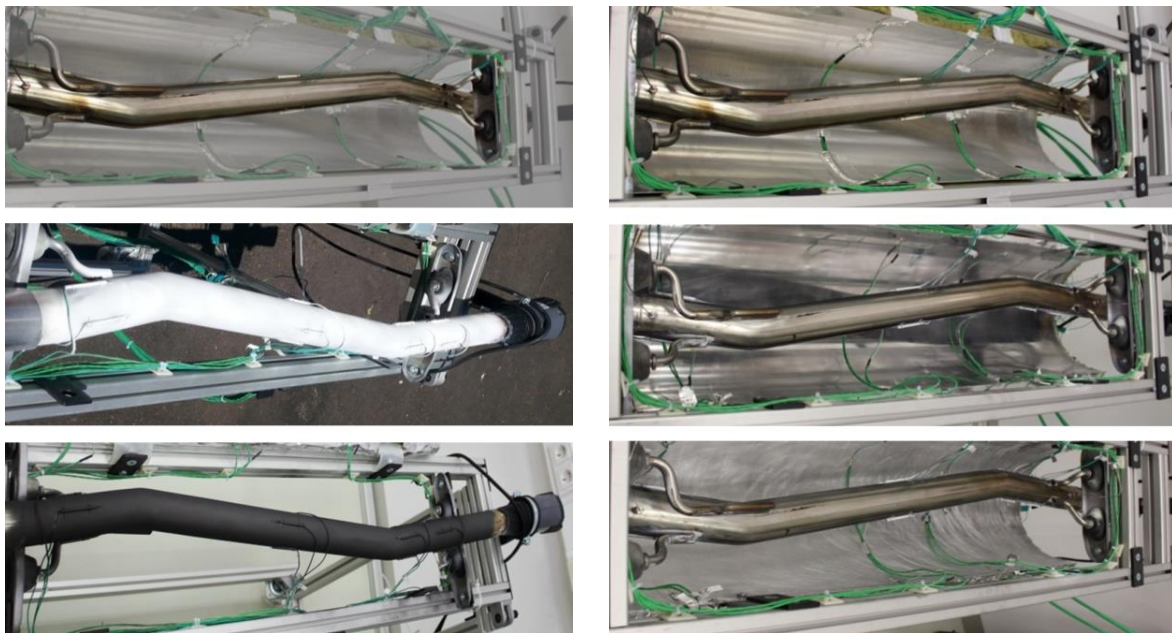


Fig. 5. Different surface colours of the tube (left) and roughness of heatshield (right).  
(full colour version available online)

As mentioned previously, the sticking method of thermocouple onto aluminum heatshield surface was also investigated, as even such a simple temperature measurement method can result in erroneous values [5]. Sticking thermocouples with aluminum adhesive tape onto aluminum heatshield surface was proved to be the best solution. The detailed description of this examination could not be presented in this work.

Our goal in the following is – after ensuring the high precision of measurements – to examine experimentally the heating up of the heatshield at inverted position beside different surface conditions, and reproduce the measured values with a 1D numerical model. By fitting the model results to the measured values, the parameters of the model (emissivities, absorption and convective heat transfer coefficients) will be determined.

### 3. Theoretical considerations and numerical model

In the first step let's focus on thermal radiation. The basic principle is stated

by the Stefan-Boltzmann law (1) which gives the radiated thermal energy [6]:

$$\dot{Q} = \varepsilon \cdot \sigma \cdot T^4 \cdot A \quad (1)$$

where  $\dot{Q}$  denotes the radiated heat flux,  $\varepsilon$  is the emissivity,  $T$  is the absolute temperature and  $A$  is the surface area of the radiating body. The absorbed radiation power can be given as equation (2):

$$\dot{Q}_{abs} = \alpha \cdot \dot{Q}_{inc} \quad (2)$$

where  $\dot{Q}_{inc}$  is the overall incident radiation and  $\alpha$  is the absorption coefficient. According to Kirchhoff's law, the emissivity ( $\varepsilon$ ) and the absorption coefficient ( $\alpha$ ) are equal for a given surface [7].

#### 3.1 Simplified numerical considerations for thermal radiation

For a rough estimation from steady-state temperature increments ( $\Delta T_G$ ,  $\Delta T_T$  and  $\Delta T_S$  see Fig. 2) of the tube-heatshield system at inverted position the following considerations

can be established:

- We assume, that the only heat input of the heatshield is the radiation from the heated tube, thus, *the input thermal energy is proportional to the emissivity* of the tube / *absorption coefficient* of the heatshield inner surface. (Heat convection and heat conduction as thermal energy inputs are negligible.)
- Taking into account the low temperature of heatshield at inverted setup (generally 5-20 degrees above room temperature) its heat loss via radiation is negligible compared to other heat loss modes. As both free convection and heat conduction are proportional to temperature difference, the *energy loss of heatshield* can be considered as being *proportional to temperature excess* over ambient temperature.
- In steady state the energy loss of heatshield is equal to its energy intake.

Based on the above assumptions, one can conclude, that the temperature increment of the heatshield ( $\Delta T_T$ ) in steady state is proportional to the emissivity of exhaust tube ( $\varepsilon$ ) or absorption coefficient of the heatshield ( $\alpha$ ) (whichever was changed), see equations (3) and (4):

$$\frac{\Delta T_{T_1}}{\Delta T_{T_2}} = \frac{\varepsilon_1}{\varepsilon_2} \quad (\text{when } \alpha = \text{const.}) \quad (3)$$

as well as:

$$\frac{\Delta T_{T_1}}{\Delta T_{T_2}} = \frac{\alpha_1}{\alpha_2} \quad (\text{when } \varepsilon = \text{const.}) \quad (4)$$

This speculation enables us to give a rough estimation to the emissivities and absorption coefficients of different surfaces from the steady-state temperatures at inverted position, however, the preconditions contain some arbitrary simplifications – as the zero thermal radiation of heatshield and the supposition of constant exhaust tube temperature – which shows the limitations of this simplified model.

### 3.2 Detailed numerical model setup

Aiming the empirical determination of emissivities / absorption ratios of different surface qualities, a 1D numerical model was built up based on elementary thermodynamics and measured data. The temperature of center cross section of heatshield during heating up was calculated parametrically from related measured temperatures and the result were fitted to directly measured temperature values. Parameter values were determined according to best fit (least sum of squares).

The heat transfer processes that were taken into account in the numerical model are visualized in Fig. 6. The calculations were made at inverted position, thus thermal convection from the tube to the heatshield could be neglected.

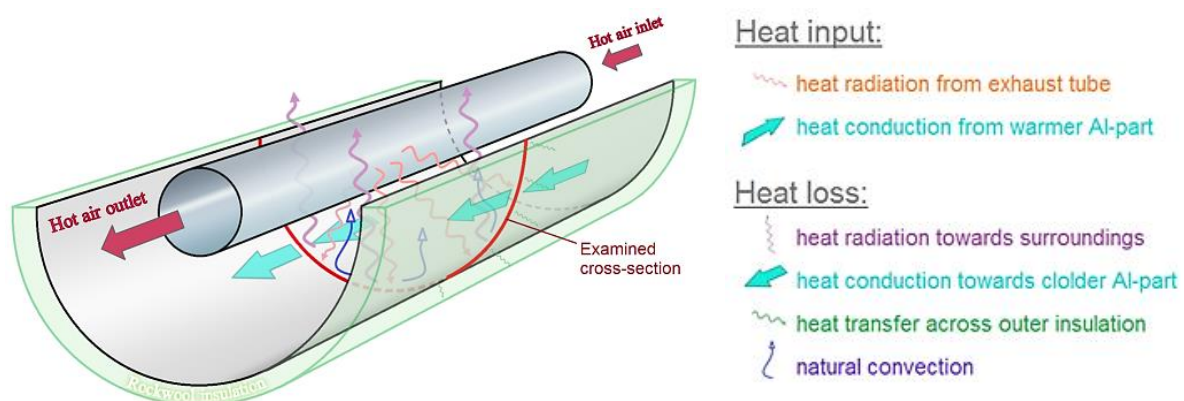


Fig. 6. Thermal components of numerical model.  
(full colour version available online)

As the heating of the tube was realized by hot air flow, its temperature is decreasing from the inlet to the outlet. It causes a temperature gradient in the heatshield too.

Heat input of the examined section of the heatshield consists of two components:

1. The thermal radiation of heated tube (irradiation);
2. Heat conduction inside the heatshield from its warmer side.

Heat loss consists of the following components:

1. Thermal radiation of heatshield (emission);
2. Free convection of warmed air;
3. Heat transfer toward outer insulation;
4. Heat conduction toward cooler side of the heatshield (hot air outlet side).

Radial direction heat gradient in the heatshield can be neglected as its width is small (1 mm) and aluminum has excellent thermal conductivity ( $205 \text{ W}\cdot\text{m}^{-1}\text{K}^{-1}$  [8]). The temperature of heatshield middle line is considered to be constant too – meaning no heat flow in tangential direction. Temperature values for calculation and validation are get from the bottom (center) line of the heatshield.

Practically, the following measured data were used during calculation:

- Ambient temperature;
- Temperature of exhaust tube surface middle (bottom) point at the middle cross section for heat irradiation;
- Temperature of heatshield surface middle (bottom) point at inlet and outlet cross section for heat conduction inside the heatshield in axial direction;
- For parameter fitting, the calculated temperature values of heat shield examined cross section were fitted to measured temperatures at its surface middle (bottom) point at middle cross section during heating up;
- The calculated instantaneous temperature of heatshield middle (examined) cross section

was used for the calculation of all other heat transfer modes.

The parameters which were determined via fitting:

- Emissivity of exhaust tube ( $\epsilon_{\text{tube}} = \alpha_{\text{tube}}$ ) beside different surface conditions (as-received, sprayed black and sprayed white);
- Absorption coefficient of heatshield ( $\alpha_{\text{shield}} = \epsilon_{\text{shield}}$ ) beside different surface conditions (as-rolled, sprayed black, sprayed white, polished and roughened);
- Convective heat transfer coefficient of heatshield ( $k_c$  or sometimes marked as  $h$ ) for free convection beside different surface conditions (as-rolled, sprayed black, sprayed white, polished and roughened).

Thermal conductivity of aluminum heat shield ( $k_{Al}$ ) and heat transfer coefficient of rock wool insulation ( $k_{ins}$ ) were taken from literature [8, 9].

### 3.3 Calculation of radiation

Thermal conduction, heat transfer through insulation and free convection were calculated according to well-known governing equations [6]. Heat radiation calculation, however, is a bit more difficult, as:

1. Emitted radiation by one part irradiates the other part at a proportion of view factor.
2. Incident radiation is partly reflected and after reflection(s) it can reach the surface again.

View factors at a pipe-half pipe setup can be determined as shown in Fig. 7. [10]

Using the data of current case, we get:  $r = 0.2455 = F_{21}$ ;  $F_{22} = 0.3441$ ;  $F_{23} = 0.4104$ .

Multiple reflections of heat radiation are of interest when calculating radiated thermal energy from exhaust tube to heatshield and the amount of emitted thermal energy by heat shield – partly backscattered by exhaust tube. To deal with this issue, the *apparent absorption coefficient* ( $\alpha_{\text{shield}}^{\text{app}}$ ) of the heatshield

is introduced, meaning the ratio of overall absorbed radiation relative to irradiation. Hereinafter heat emission toward surrounding is considered as heat loss – supposing large enough space to neglect reflections, and thermal heat transmission is set to zero for each part – thus the whole irradiation goes to absorption or reflection.

Start the consideration with the amount of heat reaching the inner surface of heat shield (considered as being uniformly dispersed):  $Q_0$  – see Fig. 8a. According to eq. (5) the amount of direct absorption equals:

$$Q_{abs1} = Q_0 \cdot \alpha_{shield} \quad (5)$$

while first reflection is given by eq. (6):

$$Q_{ref1} = 1 - Q_{abs1} = Q_0 \cdot (1 - \alpha_{shield}) \quad (6)$$

Supposing uniform reflection and using equations of Fig. 7 the backscattered radiation that reaches the central tube can be given as (7) (see Fig. 8b):

$$Q_{ref1}^{tube} = F_{21} \cdot Q_{ref1} = F_{21} \cdot Q_0 \cdot (1 - \alpha_{shield}) \quad (7)$$

while the backscattered radiation that reaches the heatshield again (8) equals:

$$Q_{ref1}^{shield} = F_{22} \cdot Q_{ref1} = F_{22} \cdot Q_0 \cdot (1 - \alpha_{shield}) \quad (8)$$

The backscattered radiation towards surroundings has no relevance for us – as mentioned above.

The amount of re-reflected radiation by tube is given by (9):

$$Q_{re-ref1}^{tube} = (1 - \alpha_{tube}) \cdot Q_{ref1}^{tube} \quad (9)$$

One problematic point is that the re-reflected radiation by tube surface ( $Q_{re-ref1}^{tube}$ )

is not dispersed uniformly to all directions (see Fig. 8/c): most of the re-reflected heat is directed backward to heatshield ( $Q_{re-ref1}^{tube \rightarrow shield}$ ) and only a smaller part is oriented to the surroundings. This ratio depends e.g. on the surface roughness (via the rate of scattering compared to straight reflection). To handle this effect we assume homogenous scattering by heatshield and suppose: that part of re-reflection is directed back toward the heatshield which reaches the bottom side of the tube – as marked in Fig. 9. Based on the indicated geometries and incident radiation surface distribution, the ratio of re-reflected radiation toward heatshield compared to the whole amount of re-reflected radiation (considered as the reflection-efficiency of the tube toward the heatshield) can be expressed as (10) (where  $r = R_{tube}/R_{shield}$ ):

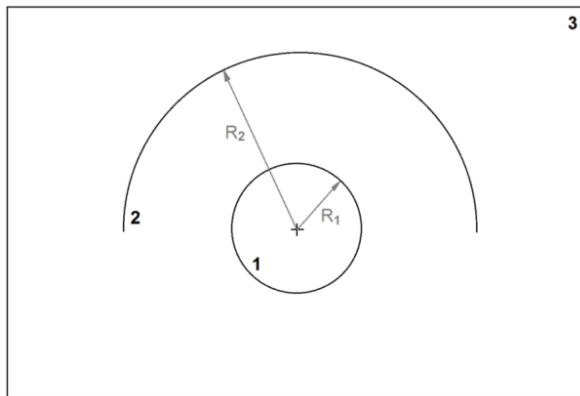
$$\begin{aligned} \eta_{tube\_ref} &= \frac{Q_{re-ref1}^{tube \rightarrow shield}}{Q_{re-ref1}^{tube}} = \\ &= 1 - \frac{\arccos(r)}{4(\arccos(r) + \arcsin(r))} \end{aligned} \quad (10)$$

Summarizing equations (5) – (10) the re-reflected radiation from the tube to the heatshield can be expressed from the original incident radiation ( $Q_0$ ) as (11):

$$Q_{re-ref1}^{tube \rightarrow shield} = Q_0 \cdot \eta_{tube\_ref} \cdot F_{21} \cdot (1 - \alpha_{tube}) \cdot (1 - \alpha_{shield}) \quad (11)$$

Adding the directly reflected radiation which reaches the heatshield directly ( $Q_{ref1}^{shield}$  see (6) and Figs. 8b and c), the overall heat radiation that was back-reflected to the heatshield during the first reflection step is given by eq. (12) as follows:

$$Q_{ref1}^{shield\ overall} = Q_0 \cdot (1 - \alpha_{shield}) \cdot (\eta_{tube\_ref} \cdot F_{21} \cdot (1 - \alpha_{tube}) + F_{22}) \quad (12)$$



$F_{xy}$  is the view factor of the radiation from x incident on y:

$$r = R_1/R_2$$

$$F_{12} = F_{13} = 0,5$$

$$F_{21} = r$$

$$F_{22} = 1 - \frac{2}{\pi} (\sqrt{1 - r^2} + r \cdot \sin^{-1} r)$$

$$F_{23} = 1 - F_{21} - F_{22}$$

Fig. 7. View factors of a tube – half-tube setup.

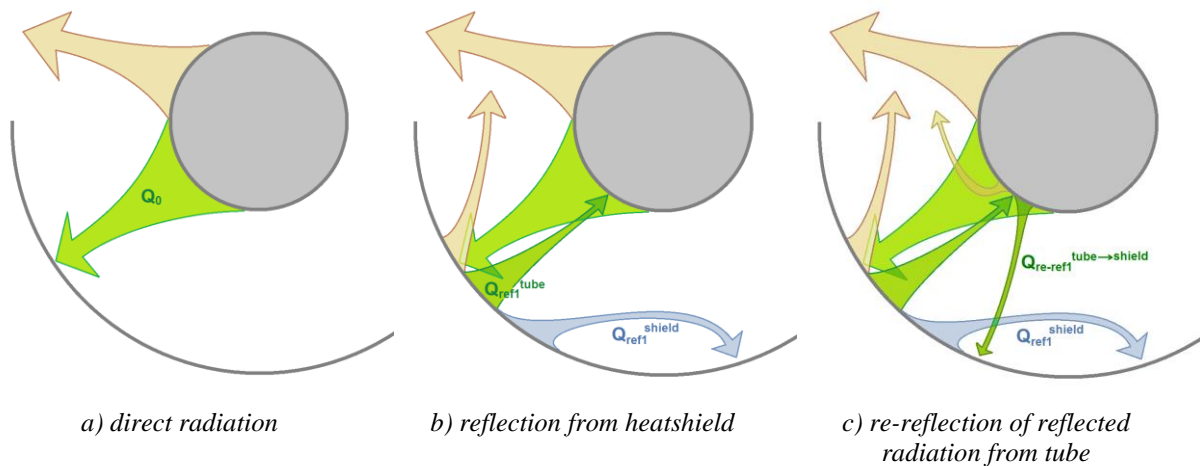


Fig. 8. Reflection of tube thermal radiation. (full colour version available online)

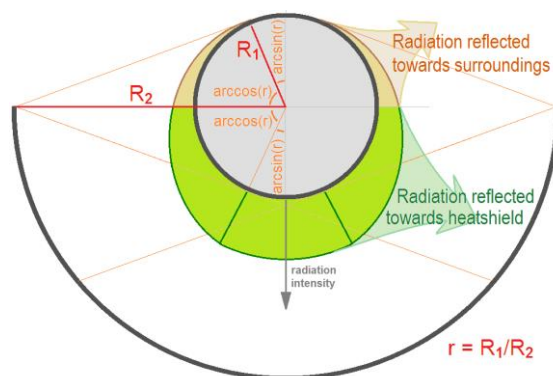


Fig. 9. Distribution of the radiated heat comes from the heatshield and back-reflected by the tube. (full colour version available online)

Substituting original incident radiation ( $Q_0$ ) by the overall first reflection we can get the amount of radiation that was backscattered to the heatshield in the second reflection step analogously. In general, the amount of radiation

that was backscattered to the heatshield after the  $n^{\text{th}}$  reflection step can be written as (13):

$$Q_{refn}^{shield\ overall} = Q_0 \cdot \left( (1 - \alpha_{shield}) \cdot (\eta_{tube\_ref} \cdot F_{21} \cdot (1 - \alpha_{tube}) + F_{22}) \right)^n \quad (13)$$

Consequently, the radiation that is absorbed by the heatshield after the  $n^{th}$  reflection step is given by equation (14):

$$Q_{abs}^{nth\ step} = \alpha_{shield} \cdot Q_0 \cdot \left( (1 - \alpha_{shield}) \cdot (\eta_{tube\_ref} \cdot F_{21} \cdot (1 - \alpha_{tube}) + F_{22}) \right)^n \quad (14)$$

The overall absorbed radiation is the sum of absorbed amounts in each step – see (15):

$$Q_{abs}^{overall} = \sum_{i=0}^{\infty} \alpha_{shield} \cdot Q_0 \cdot \left( (1 - \alpha_{shield}) \cdot (\eta_{tube\_ref} \cdot F_{21} \cdot (1 - \alpha_{tube}) + F_{22}) \right)^i \quad (15)$$

Mathematically it is the sum of a geometric series, which can be written simply as equation (16):

$$\sum Q^{shield} = \frac{\alpha_{shield} \cdot Q_0}{1 - (1 - \alpha_{shield}) \cdot (\eta_{tube\_ref} \cdot F_{21} \cdot (1 - \alpha_{tube}) + F_{22})} \quad (16)$$

We can finally express a so-called **apparent absorption coefficient** of the heatshield – given by eq. (17):

$$\alpha_{shield}^{app} = \frac{\alpha_{shield}}{1 - (1 - \alpha_{shield}) \cdot (\eta_{tube\_ref} \cdot F_{21} \cdot (1 - \alpha_{tube}) + F_{22})} \quad (17)$$

which is the ratio of the total absorbed radiation by the heatshield and the initial incident radiation.

Hereinafter, the heat absorption can be calculated from the incident radiation using apparent absorption coefficient – which incorporates all further reflections. This method simplifies calculations, thus makes parameter fitting faster and easier.

As one can see, the apparent absorption coefficient depends on the absorption coefficients of the heatshield and the tube, on the geometry through view factors ( $F_{21}$  and  $F_{22}$ ) and on the reflection efficiency ( $\eta_{tube\_ref}$ ) – latter is also a geometry-dependent variable, but surface characteristics )as e.g. diffusivity

of reflection) can also be incorporated into this parameter.

If we calculate the apparent absorption coefficient for different surfaces, we can see that it can be more than twice of the real absorption coefficient of the heatshield when both the heatshield and the exhaust tube own low absorption coefficient (high reflectivity). On the other hand, if exhaust tube is considered as a black body,  $\alpha_{shield}^{app} / \alpha_{shield}$  ratio falls into the 1...1.52 range – higher values correspond to higher reflectivity of the heatshield, resulting stronger *heatshield* → *heatshield* reflections.

The energy loss of heatshield via thermal radiation was handled in a similar manner: substituting  $Q_{refl}$  by the thermal heat emission of heatshield, all further considerations and calculations concerning reflections can be treated in the same way as described above.

### 3.4 The numerical model

The numerical model was built up along the previously described principles: the overall heat balance of the heatshield middle line was constructed. The base equation (18) declares the balance of input-, egressed and stored energies (heat amount per unit time) per unit mass:

$$\Delta \dot{E} = \dot{Q}_{input} - \dot{Q}_{output} \quad (18)$$

where  $\Delta E$  denotes the stored thermal energy via temperature increase (heat capacity).

Explicating the components of (18) equation (19) is resulted:

$$C_{p\ Al} \cdot \Delta \dot{T}_S = \dot{Q}_{cond}^{tot} + \dot{Q}_{rad}^{tot} - \dot{Q}_{ins} - \dot{Q}_{conv} \quad (19)$$

with the nomenclature:

$Q_{cond}^{tot}$ : Total heat input energy via heat conduction of heatshield aluminum (heat input from warmer side minus heat output toward cooler side of heatshield)

$Q_{rad}^{tot}$ : Total radiated energy input (irradiation from exhaust tube minus thermal emission by shield);

$Q_{ins}$ : Heat loss through outer insulation of the heatshield;

$Q_{conv}$ : Heat loss via free convection;

$C_{p Al}$ : The specific heat capacity of aluminum (heatshield material);

$\Delta T_S$ : The rate of temperature-increase of heatshield.

Numerical model was based on equation (19) with a time step of 0.5 s and total heating time of 3600 s.

The values (parameters, constant and measured values) that were used during calculations are listed in Table 1.

The numerical model was built up in Microsoft Excel with a time step equal to measurement (0.5 s). After giving initial values (given in Table 1. in braces after each variable) the variables were optimized so as to reach minimum difference (sum of squares) between measured and calculated temperature values of heatshield at examined point. To compensate the high number of measured values at stationary state compared to that of heating ramp, relative differences were used for the fitting – normalized by temperature increase relative to initial temperature.

Optimization processes were executed by Solver module using nonlinear GRG (gradient) method using adjacent differences and  $10^{-4}$  convergence criterion.

Table 1

*List of numerical values used for calculation.*

Name / Description	Notation	Value
<b>Constants – Geometrical properties</b>		
Radius of heated tube	$R_1$	0.027 m
Radius of heatshield	$R_2$	0.11 m
Distance of sections 1 and 3 from the middle section	-	0.28 m
Heatshield insulation thickness	-	0.03 m
Heatshield aluminum sheet thickness	-	0.001 m
Calculated view factors from the setup's geometry	-	see Fig. 7.
<b>Constants – Thermal and physical properties</b>		
Conductivity of aluminum	$k_{Al}$	205 W.mK <sup>-1</sup>
Specific heat capacity of aluminum	$C_p$	897 J.kg <sup>-1</sup> .K <sup>-1</sup>
Density of aluminum	$\rho_{Al}$	2700 kg.m <sup>-3</sup>
Stefan-Boltzmann-constant	$\sigma$	$5.67 \cdot 10^{-8}$ W.m <sup>-2</sup> .K <sup>-4</sup>
<b>Variables – Emissivity and convective heat transfer coefficient of different surfaces (values given in brackets are initial values of parameter fitting according to [11])</b>		
Emissivity of as-received exhaust tube	$\epsilon$	(0.5)
Emissivity of black-sprayed exhaust tube	$\epsilon$	(0.97)
Emissivity of white-sprayed exhaust tube	$\epsilon$	(0.6)
Emissivity of as-rolled aluminum heatshield	$\epsilon$	(0.09)
Emissivity of black-sprayed aluminum heatshield	$\epsilon$	(0.8)
Emissivity of white-sprayed aluminum heatshield	$\epsilon$	(0.6)
Emissivity of roughened aluminum heatshield	$\epsilon$	(0.2)
Emissivity of polished aluminum heatshield	$\epsilon$	(0.06)
Convective heat transfer coefficient of as-rolled heatshield	$k_c$	(5)
Convective heat transfer coeff. of white coated heatshield	$k_c$	(5)
Convective heat transfer coeff. of black coated heatshield	$k_c$	(5)
Convective heat transfer coeff. of roughened heatshield	$k_c$	(10)
Convective heat transfer coeff. of polished heatshield	$k_c$	(5)
<b>Measured values</b>		
Ambient temperature (for the calculation of emitted heat of heatshield)		
Temperature of exhaust tube surface middle point at middle section (above examined heatshield area, for radiated heat calculation)		
Temperature of heatshield at the inlet and at the outlet section (for conducted heat input and output calculation)		

#### 4. Results and discussion

As described above, exact surface thermal radiation and convection properties were determined by fitting numerical model (described in Chapter 3.2) to measured temperature data. To illustrate this method, two results were shown in Figs. 10 and 11 - for base (unmodified) surfaces and for black coated tube and heatshield surfaces, respectively. Despite the not totally accurate fit, the typical difference of measured and calculated values does not exceed  $0.2^{\circ}\text{C}$ , the standard deviation of relative error is 0.04 for the unmodified surfaces (keep in mind the logarithmic axis of temperature!). The situation of black tube and black heatshield is even better: in this case the fitting follows quite

accurately the measurements: typical difference of measured and calculated values are within  $0.1^{\circ}\text{C}$ , the standard deviation of relative error is 0.01.

The accuracy of fitting depends mostly on the reflectivity of the surfaces: the model describes most accurately the homogeneously scattering, highly absorbing surfaces (with lower ratio of reflection).

As described above, calculation fitting was executed via parameter optimization resulting refined values of emissivities, absorption coefficients and convective heat transfer coefficients (of heatshield) for different surfaces. However, due to industrial secret, direct numerical data could not be presented in this paper.

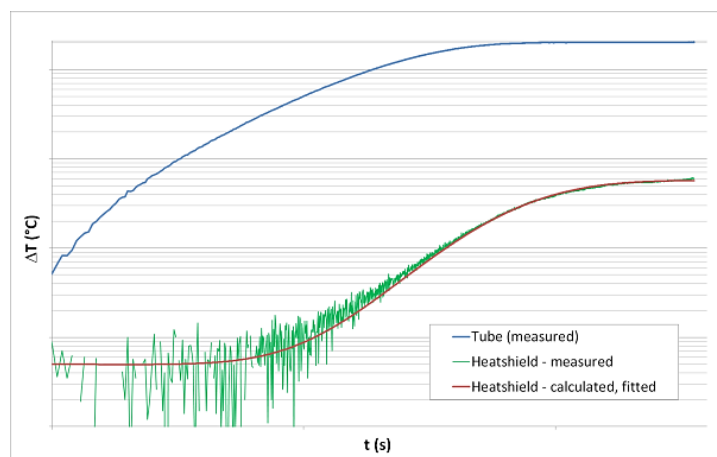


Fig. 10. Measured and calculated temperature data of tube and heatshield – both with as-received surface. (full colour version available online)

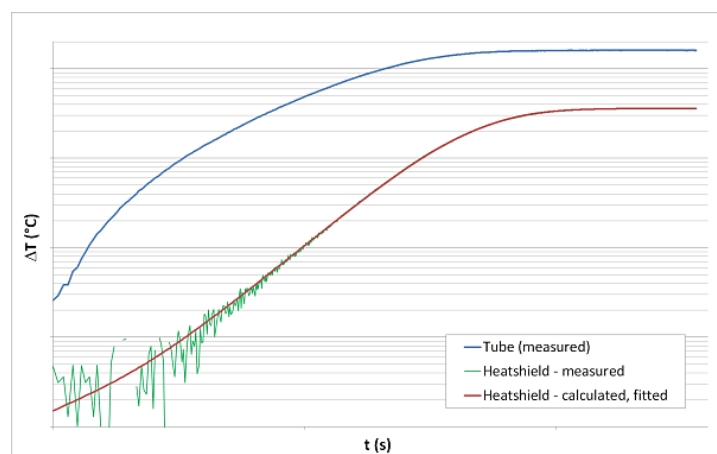


Fig. 11. Measured and calculated temperature data of tube and heatshield – both with black coated surface. (full colour version available online)

## 5. Conclusions

A simplified setup of car exhaust tube – heat shield system was designed and built. Using this equipment different aspects of heat transfer processes were investigated. Heat radiation and free convection were set in the focus; their effects were uncoupled by using the system in upside-down (inverted) position. A simplified theory was developed for rough estimations from steady state temperatures of the system, as like as a more complex numerical model was built up aiming the determination of the system's thermal properties via fitting calculated data to measured ones.

The most important findings are:

1. Using well-parameterizable and flexible measurement setup, the thermal radiation and convection effects were successfully decoupled and different surfaces were examined.
2. A detailed numerical model was created, which incorporates heat conduction, convection and radiation too. By introducing apparent absorption coefficient, multiple reflections were handled in a convenient and effective way.
3. The thermal properties of tube and heatshield were determined by fitting the calculation to measurement data via parameter optimization. Low fitting deviation implies that the numerical model was built up in an adequate way. Fitting error and theoretical consideration equally prove that the numerical model gives the best results for highly absorptive/diffusively reflective surfaces – as e.g. porous coatings.
4. Results are usually in good accordance with literature data however, we get slightly different (presumably more accurate) values for some surfaces (e.g. for matte white and black coatings).
5.  $k_c$  values for free convection above heat shield were also determined, which are in good accordance with expectations.

Considering the results and issues that emerged during examinations the following additional tasks are planned in the near future:

1. Reconstruct the measuring equipment for making it suitable for higher tube-surface temperature (up to 600°C).
2. Thorough examination of free convection in normal setup (heatshield above tube).
3. Measuring on real automotive heatshield (embossed aluminum sheet).
4. Building up CFD and radiation simulation models, which should be developed and validated according to measurements.

## References

- [1] S. Yang, D. Wang, Y. Dang, L. Li: SAE International (2015), doi: 10.4271/2015-01-2902.
- [2] F. Fortunato, M. Caprio, P. Oliva, G. D'Aniello, P. Pantaleone, A. Andreozzi, O. Manca: SAE International (2007), doi:10.4271/2007-01-1094.
- [3] A.C. Alkidas, P.A. Battiston, D.J. Kapparos: SAE International (2004), doi: 10.4271/2004-01-0050.
- [4] T. Binner, H. Reister, E.P. Weidmann, J. Wiedemann: Aspects of Underhood Thermal Analyses, Progress in Vehicle Aerodynamics IV: Numerical Methods, Tagungsband KFZ-Aerodynamik (Research Institute of Automotive Engineering and Vehicle Engines Stuttgart (FKFS)) 2006.
- [5] C. Hochenauer, J. Wurm: Smart Science 2(3) (2014) 116-125.
- [6] John H. Leinhard IV and John H. Leinhard V: A heat transfer textbook, Phlogiston Press, Cambridge, Massachusetts, 2008.
- [7] Max Planck: The theory of Heat Radiation, P. Blakiston's Son & Co., Philadelphia, 1914.
- [8] [http://www.engineeringtoolbox.com/thermal-conductivity-d\\_429.html](http://www.engineeringtoolbox.com/thermal-conductivity-d_429.html).
- [9] Rockwool datasheet, [http://www.rockwool.gr/files/RW-GR/Product%20range/Industrial/Rockwool\\_Larock%2040%20ALS.pdf](http://www.rockwool.gr/files/RW-GR/Product%20range/Industrial/Rockwool_Larock%2040%20ALS.pdf).
- [10] I. Martínez: Radiative view factors – educational material, Technical University of Madrid, Department of Propulsion and Thermal Fluid Dynamic, <http://webserver.dmt.upm.es/~isidoro/tc3/Radiation%20View%20factors.pdf>.
- [11] <http://www.infrared-thermography.com/material.htm>



# OPTIMIZATION OF SOLID-STATE SYNTHESIS PROCESS OF ADVANCED CERAMIC MATERIALS: INFLUENCE OF MIXING CONDITIONS

Sakri Adel<sup>1,\*</sup>

<sup>1</sup> Industrial chemistry department, University of Biskra, box 145 RP Biskra (07000) Algeria

\*corresponding author: e-mail: adelsak@yahoo.fr

## Resume

In this paper, the effect of mixing process on solid state reaction of solid oxide material mixture was studied. Lead piezoelectric ceramic specimens  $0.5 \text{Pb}(\text{Zn}_{1/3}, \text{Sb}_{2/3})\text{O}_3 - 0.5 \text{Pb}_{0.98}\text{La}_{0.02}(\text{Zr}_{0.48}, \text{Ti}_{0.52})\text{O}_3$  prepared by different mixing procedures, were conducted under different conditions such as order, combination and mixing time. The phase formation, composition nature, structural properties of powder mixture was analyzed by X-ray diffraction. The obtained results for different mixing processes make the solid state reaction method more selective, taking into consideration the attraction forces between the reactants and the electronegativity of oxide reactants.

## Article info

### Article history:

Received 13 May 2016

Accepted 22 August 2016

Online 22 October 2016

### Keywords:

Solid state reaction method;

Mixing process;

Solid attraction;

Electronegativity;

X-ray diffraction.

Available online: <http://fstroj.uniza.sk/journal-mi/PDF/2016/14-2016.pdf>

ISSN 1335-0803 (print version)

ISSN 1338-6174 (online version)

## 1. Introduction

The most widely used piezoelectric ceramics for these applications are those based on lead titanate zirconate  $x \text{PbZrO}_3 - (1-x) \text{PbTiO}_3$  solid solution, also known as PZT, because of their good properties and the wide possibilities to modify their structure and properties using various dopants [1, 2].

Different methods were developed to synthesize ceramic powders, including chemical and physical processes [3, 4]. The simplest physical method is the mechanical milling, where mechanical action is used to refine the powders [5 - 8]. In comparison, chemical process, such as solid-state reaction and various wet-chemical solution routes are the most widely employed to synthesize advanced ceramics in general [9, 10]. For solid-state reaction methods, the use of high energy milling in recent years has shown certain advantages in reducing the phase formation temperatures of ceramic materials, because transparent ceramics have

usually relatively high reaction temperatures [11, 12].

The comparison between the different synthesis methods, leads to conclude that the solid state reaction method is characterized by poor control of composition, morphology and reactivity [13, 14].

In this paper, an attempt has been made to systematically study the effect of different mixing processes for the solid state reaction method on the structural properties of PZS-PLZT ceramics. The samples were synthesized by solid state reaction method, their nature; structural properties and selectivity were investigated.

## 2. Experimental

For this study,  $(1-x)\text{PZS}-x\text{PLZT}$  system was chosen [15, 16], with  $0.5\text{Pb}(\text{Zn}_{1/3}, \text{Sb}_{2/3})\text{O}_3 - 0.5\text{Pb}_{0.98}\text{La}_{0.02}(\text{Zr}_{0.48}, \text{Ti}_{0.52})\text{O}_3$  composition. It was synthesized from high purity oxide powders namely, PbO (99.90 % purity),  $\text{ZrO}_2$  (99.90 % purity),  $\text{TiO}_2$  (99.80 % purity), ZnO (99.90 %

purity) from Sigma Aldrich,  $\text{Sb}_2\text{O}_3$  (99.90 % purity) and  $\text{La}_2\text{O}_3$  (99.90 % purity) from Alfa Aesar. The samples were prepared by the conventional ceramic process (solid-state method) using four different mixing combinations (see table 1 processes 1, 2, 3, 4, 5, 6, 7 and 8). Stoichiometric amounts of metal oxides were mixed, ball-milled, and calcined at  $800\text{ }^\circ\text{C}$  ( $2\text{ }^\circ\text{C}/\text{min}$ ) for 120 min. The calcined powder was then ball-milled for 4 hours until very fine (small) particles are obtained. After drying, the powder was pressed and disk-like shaped then sintered at  $1200\text{ }^\circ\text{C}$  (heating rate =  $2\text{ }^\circ\text{C}/\text{min}$ ) during two hours in a closed alumina crucible using a high temperature programmable furnace. It is to be noted that a lead loss is possible by evaporation of  $\text{PbO}$  which is very volatile at  $T \geq 900\text{ }^\circ\text{C}$ . To limit this effect; a  $\text{PbO}$  overloaded medium was maintained with  $\text{PbZrO}_3$  powder to reduce this loss during sintering. A Bruker-axe X-ray diffraction analyzer, D8 with  $\text{Cu K}\alpha$  radiation ( $\lambda = 1.5406\text{ \AA}$ ) was used. The presence of perovskite structure and phase composition in samples were detected by Rietveld method using the crystallographic and geometric properties of resulting compounds.

### 3. Mixing combinations

In every process, each oxide should be mixed in an alcohol medium for two hours at  $100\text{ }^\circ\text{C}$ . After that, every two oxides were mixed and stirred in the same conditions. Finally, the resulting three mixtures (each mixture containing two oxides which were already agitated) were mixed and stirred in an alcohol medium for two hours at  $100\text{ }^\circ\text{C}$ . The final mixture was milled for 30 minutes; then stirred during the same period and finally milled again for two hours. Eight mixing processes based on the choice of the addition order of oxides for the mixing operation were proposed (see Table 1 process 1, 2, 3, 4, 5, 6, 7 and 8).

### 4. Results and discussion

The purity and crystallinity of the synthesized samples were further examined

by the powder XRD technique. The XRD patterns of the  $0.5\text{Pb}(\text{Zn}_{1/3}, \text{Sb}_{2/3})\text{O}_3\text{-}0.5\text{Pb}_{0.98}\text{La}_{0.02}(\text{Zr}_{0.48}, \text{Ti}_{0.52})\text{O}_3$  specimens sintered at  $1200\text{ }^\circ\text{C}$  after using different mixing procedure are shown in Fig. 1 (process 1, 2, 3, 4, 5, 6, 7 and 8). The different mixing procedures obviously affected the nature and the microstructure properties of sintered samples.

The obtained compounds (phases) with quantification percentage are shown in Table 2. Varying the mixing procedure affects chemical kinetic formation of resulting compounds. This may be due to the attraction forces between different solid powder reactants [17 - 19].

Fig. 2 shows the quantitative percentage of PZT and PLZT depending on the mixing procedure. The results reveal that the mixing procedure influenced the nature of formed compound. The mixing processes (1, 3, 5, 6, 7 and 8) led to produce the PZT compounds, while (2) and (4) processes were found to lead to PLZT compounds. It can be seen that the mixing process can provide greater selectivity in the reaction system.

Obviously, the mixing procedures influence not only the nature of the phase and microstructure, but also Zr/Ti composition. As for the mixing procedures (1, 2, 5, 6, 7 and 8), the percentage of zirconium is greater than that of titanium in the formed phases. But for the third and fourth processes (3, 4), the Zr percentage was found less than that of Ti (see Table 3).

The total electronegativity of the oxide ( $E_{ox}$ ) was determined by Portier using the following equation (1) [20, 21]:

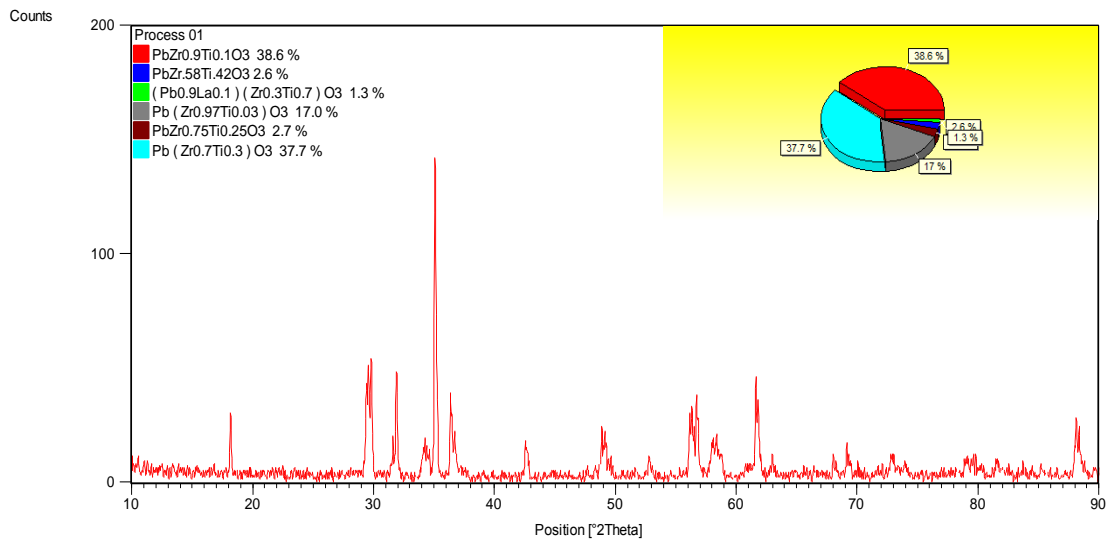
$$E_{ox} = ((X_M)^m * (X_O)^n)^{1/(m+n)} \quad (1)$$

Where  $X_M$  and  $X_O$  are the electronegativities of the cation and oxygen anion, respectively, and  $m$  is the stoichiometry of the cation in the oxide while  $n$  is the stoichiometry of the oxygen anion in the oxide. So the Table 4 shows the approximate values of ( $E_{ox}$ ) (oxide reactant electronegativity) and mass composition of the samples.

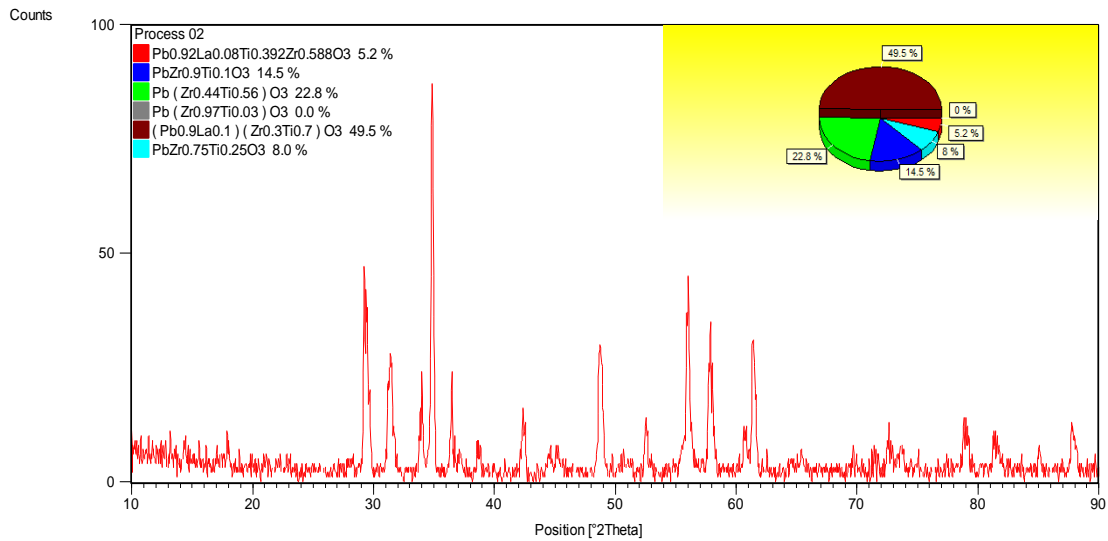
Table 1

*Different mixing process.*

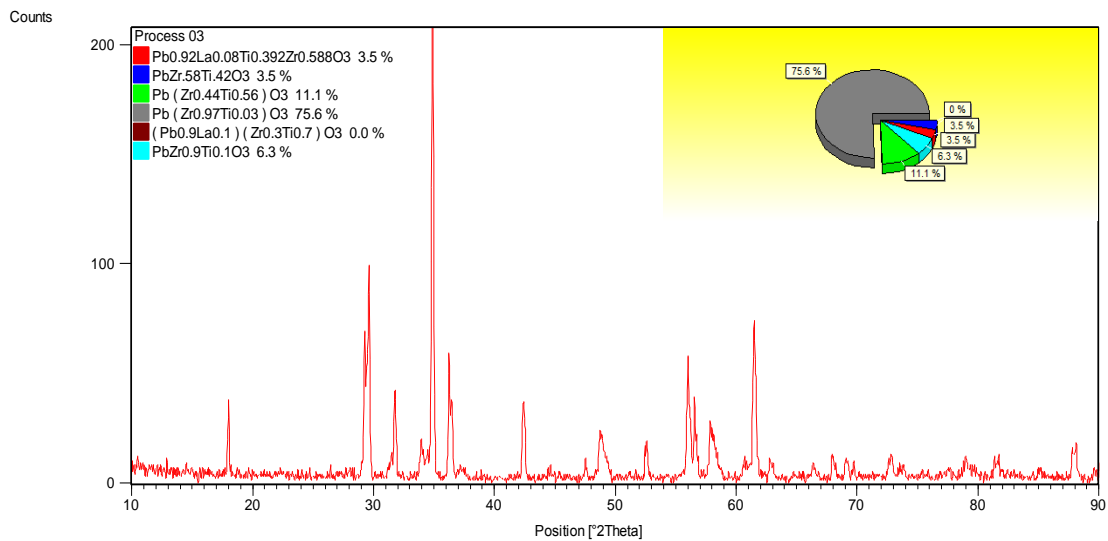
	Process 01	Process 02	Process 03	Process 04	Process 05	Process 06	Process 07	Process 08
<b>Step 01:</b> Agitation at 100°C in alcohol medium (2hours), for each oxide	PbO;TiO <sub>2</sub> ZrO <sub>2</sub> ;Sb <sub>2</sub> O <sub>3</sub> ZnO;La <sub>2</sub> O <sub>3</sub>	PbO;TiO <sub>2</sub> ZrO <sub>2</sub> ;Sb <sub>2</sub> O <sub>3</sub> ZnO;La <sub>2</sub> O <sub>3</sub>	PbO;TiO <sub>2</sub> ZrO <sub>2</sub> ;Sb <sub>2</sub> O <sub>3</sub> ZnO;La <sub>2</sub> O <sub>3</sub>	PbO;TiO <sub>2</sub> ZrO <sub>2</sub> ;Sb <sub>2</sub> O <sub>3</sub> ZnO;La <sub>2</sub> O <sub>3</sub>	PbO;TiO <sub>2</sub> ZrO <sub>2</sub> ;Sb <sub>2</sub> O <sub>3</sub> ZnO;La <sub>2</sub> O <sub>3</sub>	PbO;TiO <sub>2</sub> ZrO <sub>2</sub> ;Sb <sub>2</sub> O <sub>3</sub> ZnO;La <sub>2</sub> O <sub>3</sub>	PbO;TiO <sub>2</sub> ZrO <sub>2</sub> ;Sb <sub>2</sub> O <sub>3</sub> ZnO;La <sub>2</sub> O <sub>3</sub>	PbO;TiO <sub>2</sub> ZrO <sub>2</sub> ;Sb <sub>2</sub> O <sub>3</sub> ZnO;La <sub>2</sub> O <sub>3</sub>
<b>Step 02:</b> Mixing at 100°C in alcohol medium (2hours)	(PbO+TiO <sub>2</sub> ); (ZrO <sub>2</sub> +Sb <sub>2</sub> O <sub>3</sub> ); (ZnO+La <sub>2</sub> O <sub>3</sub> )	(PbO+La <sub>2</sub> O <sub>3</sub> ); (ZrO <sub>2</sub> +Sb <sub>2</sub> O <sub>3</sub> ); (ZnO+ TiO <sub>2</sub> )	(PbO+Sb <sub>2</sub> O <sub>3</sub> ); (ZrO <sub>2</sub> +La <sub>2</sub> O <sub>3</sub> ); (ZnO+ TiO <sub>2</sub> )	(PbO+La <sub>2</sub> O <sub>3</sub> ); (ZrO <sub>2</sub> +TiO <sub>2</sub> ); (ZnO+Sb <sub>2</sub> O <sub>3</sub> )	(La <sub>2</sub> O <sub>3</sub> +Sb <sub>2</sub> O <sub>3</sub> ); (ZnO+ TiO <sub>2</sub> ); (ZrO <sub>2</sub> + PbO)	(ZrO <sub>2</sub> +La <sub>2</sub> O <sub>3</sub> ); (PbO+Sb <sub>2</sub> O <sub>3</sub> )	(ZrO <sub>2</sub> +La <sub>2</sub> O <sub>3</sub> )  (ZrO <sub>2</sub> +La <sub>2</sub> O <sub>3</sub> + TiO <sub>2</sub> )  (ZrO <sub>2</sub> +La <sub>2</sub> O <sub>3</sub> + TiO <sub>2</sub> +ZnO)  (ZrO <sub>2</sub> +La <sub>2</sub> O <sub>3</sub> + TiO <sub>2</sub> +ZnO+ Sb <sub>2</sub> O <sub>3</sub> )	(PbO+Sb <sub>2</sub> O <sub>3</sub> )  (PbO+Sb <sub>2</sub> O <sub>3</sub> +ZnO)  (PbO+Sb <sub>2</sub> O <sub>3</sub> +ZnO+ TiO <sub>2</sub> )  (PbO+Sb <sub>2</sub> O <sub>3</sub> +ZnO+ TiO <sub>2</sub> +ZrO <sub>2</sub> )
<b>Step 03:</b> Milling for (2hours)	(PbO+TiO <sub>2</sub> ); (ZrO <sub>2</sub> +Sb <sub>2</sub> O <sub>3</sub> ); (ZnO+La <sub>2</sub> O <sub>3</sub> )	(PbO+La <sub>2</sub> O <sub>3</sub> ); (ZrO <sub>2</sub> +Sb <sub>2</sub> O <sub>3</sub> ); (ZnO+ TiO <sub>2</sub> )	(PbO+Sb <sub>2</sub> O <sub>3</sub> ); (ZrO <sub>2</sub> +La <sub>2</sub> O <sub>3</sub> ); (ZnO+ TiO <sub>2</sub> )	(PbO+La <sub>2</sub> O <sub>3</sub> ); (ZrO <sub>2</sub> +TiO <sub>2</sub> ); (ZnO+Sb <sub>2</sub> O <sub>3</sub> )	(La <sub>2</sub> O <sub>3</sub> +Sb <sub>2</sub> O <sub>3</sub> ); (ZnO+ TiO <sub>2</sub> ); (ZrO <sub>2</sub> + PbO)	(ZrO <sub>2</sub> +La <sub>2</sub> O <sub>3</sub> ); (PbO+Sb <sub>2</sub> O <sub>3</sub> )		
<b>Step 04:</b> Mixing at 100°C in alcohol medium (2hours)	(PbO+TiO <sub>2</sub> + ZrO <sub>2</sub> +Sb <sub>2</sub> O <sub>3</sub> + ZnO+La <sub>2</sub> O <sub>3</sub> )	(PbO+La <sub>2</sub> O <sub>3</sub> + ZrO <sub>2</sub> +Sb <sub>2</sub> O <sub>3</sub> + ZnO+ TiO <sub>2</sub> )	(PbO+Sb <sub>2</sub> O <sub>3</sub> + ZrO <sub>2</sub> +La <sub>2</sub> O <sub>3</sub> + ZnO+ TiO <sub>2</sub> )	(PbO+La <sub>2</sub> O <sub>3</sub> + ZrO <sub>2</sub> +TiO <sub>2</sub> + ZnO+Sb <sub>2</sub> O <sub>3</sub> )	(La <sub>2</sub> O <sub>3</sub> +Sb <sub>2</sub> O <sub>3</sub> + ZnO+ TiO <sub>2</sub> + ZrO <sub>2</sub> + PbO)	(ZrO <sub>2</sub> +La <sub>2</sub> O <sub>3</sub> +TiO <sub>2</sub> ); (ZnO+PbO+Sb <sub>2</sub> O <sub>3</sub> )	(ZrO <sub>2</sub> +La <sub>2</sub> O <sub>3</sub> + TiO <sub>2</sub> +ZnO+ Sb <sub>2</sub> O <sub>3</sub> +PbO)	(PbO+Sb <sub>2</sub> O <sub>3</sub> +ZnO+ TiO <sub>2</sub> +ZrO <sub>2</sub> + La <sub>2</sub> O <sub>3</sub> )
<b>Step 05:</b>			Milling in alcohol medium for (0.5hour) : (PbO+TiO <sub>2</sub> +ZrO <sub>2</sub> +Sb <sub>2</sub> O <sub>3</sub> +ZnO+La <sub>2</sub> O <sub>3</sub> )					
<b>Step 06:</b>			Mixing in alcohol medium (2hours) : (PbO+TiO <sub>2</sub> +ZrO <sub>2</sub> +Sb <sub>2</sub> O <sub>3</sub> +ZnO+La <sub>2</sub> O <sub>3</sub> )					
<b>Step 07:</b>			Milling in alcohol medium for (2hours) : (PbO+TiO <sub>2</sub> +ZrO <sub>2</sub> +Sb <sub>2</sub> O <sub>3</sub> +ZnO+La <sub>2</sub> O <sub>3</sub> )					
<b>Step 08:</b>			Calcination at 800°C : (PbO+TiO <sub>2</sub> +ZrO <sub>2</sub> +Sb <sub>2</sub> O <sub>3</sub> +ZnO+La <sub>2</sub> O <sub>3</sub> )					



a) mixing procedure 1

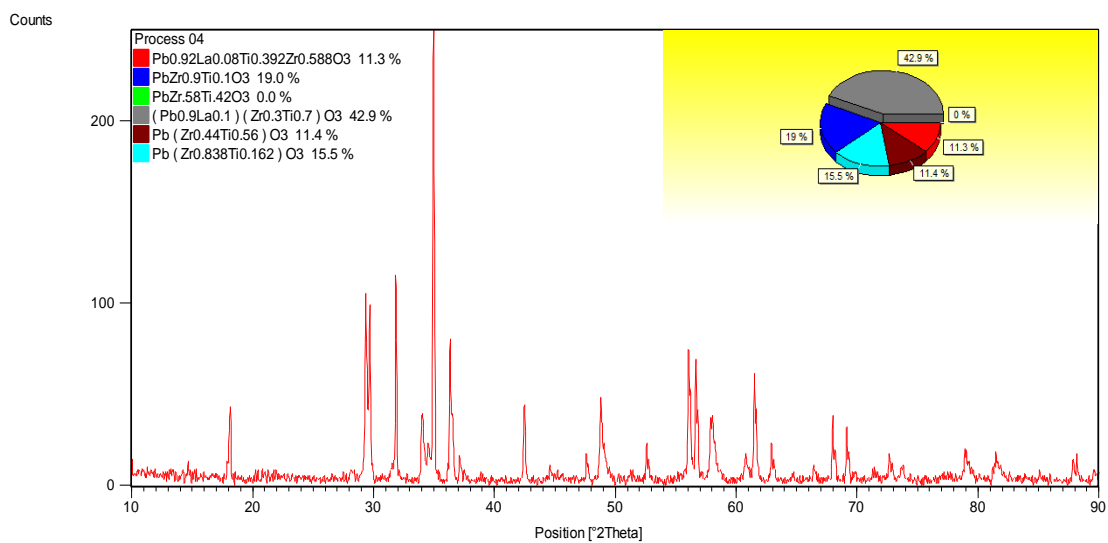


b) mixing procedure 2

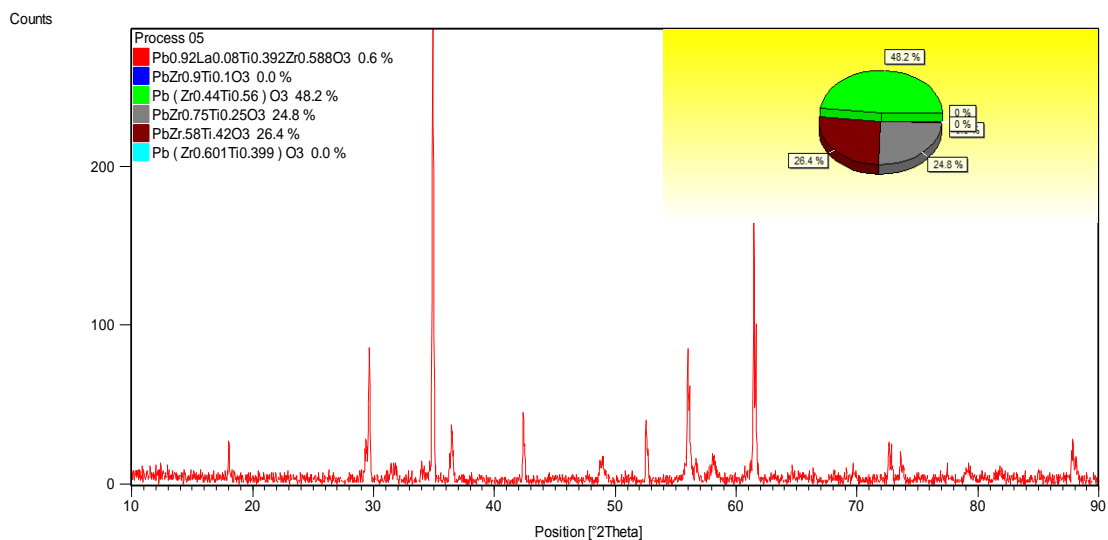


c) mixing procedure 3

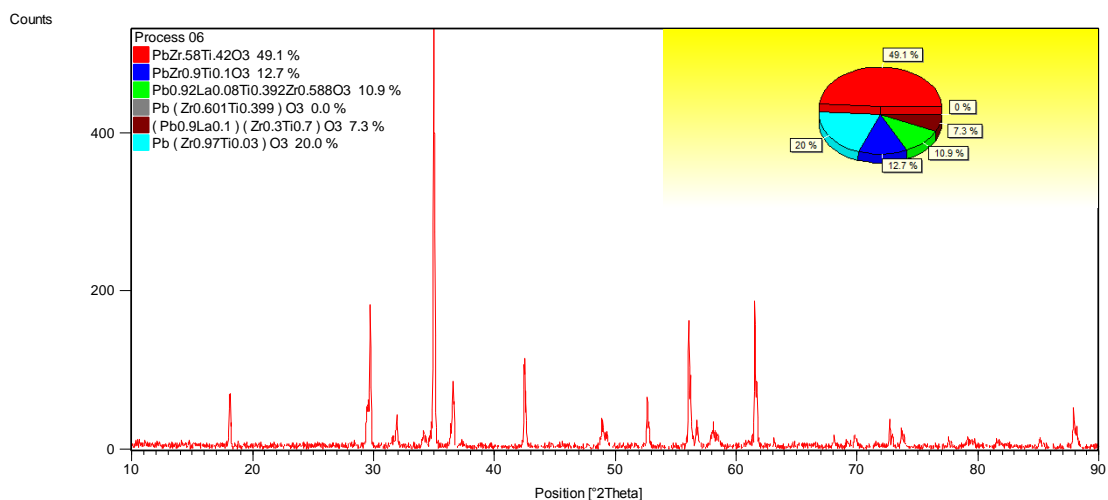
Fig. 1. XRD patterns of sintered samples for different mixing procedures 1, 2, 3, 4, 5, 6, 7, and 8.  
(full colour version available online)



d) mixing procedure 4

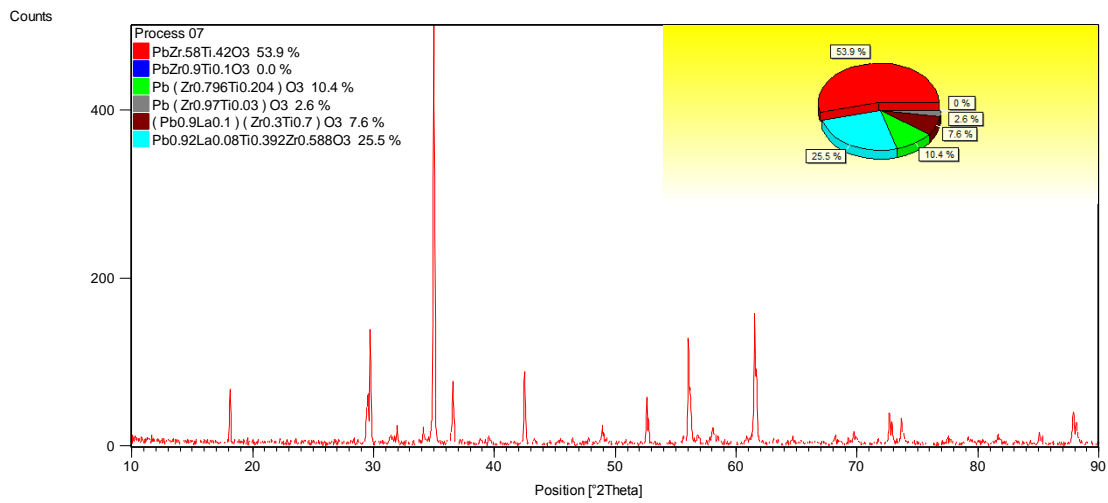


e) mixing procedure 5

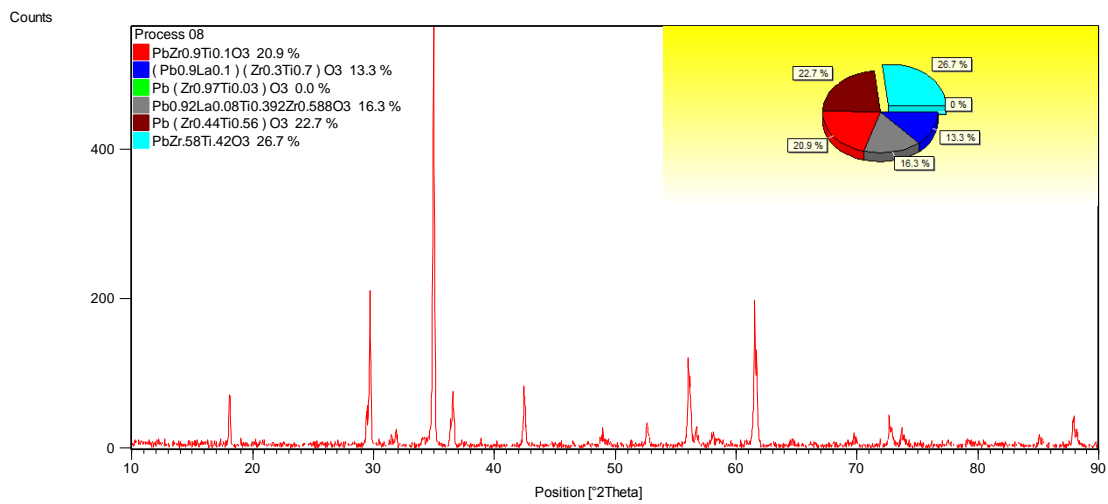


f) mixing procedure 6

Continuing of Fig. 1. XRD patterns of sintered samples for different mixing procedures 1, 2, 3, 4, 5, 6, 7, and 8.  
(full colour version available online)



g) mixing procedure 7



h) mixing procedure 8

Continuing of Fig. 1. XRD patterns of sintered samples for different mixing procedures 1, 2, 3, 4, 5, 6, 7, and 8. (full colour version available online)

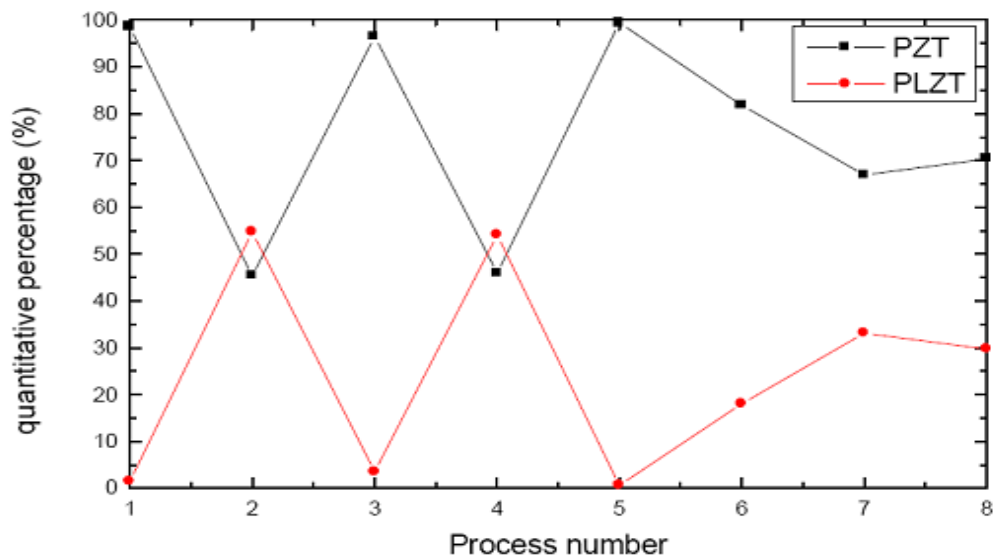


Fig. 2. Quantitative percentage of PLZT and PZT as a function of mixing process.

Table 2

*Relative quantitative percentage of PZT and PLZT formed phases (relative to all the obtained PZT based phases) as a function of mixing process.*

Resulting compounds	quantitative percentage							
	Process 1	Process 2	Process 3	Process 4	Process 5	Process 6	Process 7	Process 8
$Pb(Zr_{0.9}Ti_{0.1})O_3$	38.6%	14.5%	6.3%	19%	0%	12.7%	0%	20.9%
$Pbt(Zr_{0.58}Ti_{0.42})O_3$	2.6%	0%	3.5%	0%	26.4%	49.1%	53.9%	26.7%
$(Pb_{0.9}La_{0.1})(Zr_{0.3}Ti_{0.7})O_3$	1.3%	49.5%	0%	42.9%	0%	7.3%	7.6%	13.3%
$Pb(Zr_{0.97}Ti_{0.03})O_3$	17%	0%	75.6%	0%	0%	20%	2.6%	0%
$Pb(Zr_{0.75}Ti_{0.25})O_3$	2.7%	8%	0%	0%	24.8%	0%	0%	0%
$Pb(Zr_{0.7}Ti_{0.3})O_3$	37.7%	0%	0%	0%	0%	0%	0%	0%
$(Pb_{0.92}La_{0.08})(Ti_{0.392}Zr_{0.588})O_3$	0%	5.2%	3.5%	11.3%	0.6%	10.9%	25.5%	16.3%
$Pb(Zr_{0.44}Ti_{0.56})O_3$	0%	22.8%	11.1%	11.4%	48.2%	0%	0%	22.7%
$Pb(Zr_{0.838}Ti_{0.162})O_3$	0%	0%	0%	15.5%	0%	0%	0%	0%
$Pb(Zr_{0.601}Ti_{0.399})O_3$	0%	0%	0%	0%	0%	0%	0%	0%
$Pb(Zr_{0.796}Ti_{0.204})O_3$	0%	0%	0%	0%	0%	0%	10.4%	0%
<b>Total</b>	<b>≈100%</b> <b>(99.9%)</b>	<b>≈100%</b>	<b>≈100%</b>	<b>≈100%</b> <b>(100.1%)</b>	<b>≈100%</b>	<b>≈100%</b>	<b>≈100%</b>	<b>≈100%</b> <b>(99.9%)</b>

Table 3

*Percentage of Zr and Ti in the PZT and PLZT phases formed as a function of mixing process.*

$$Q_{\%Zr > \%Ti} = \left[ \sum \%Pb(Zr_x, Ti_y) + \sum \%PbLa(Zr_{x'}, Ti_{y'}) \right] \text{ with: } x > y \text{ and } x' > y'$$

$$Q_{\%Ti > \%Zr} = \left[ \sum \%Pb(Zr_x, Ti_y) + \sum \%PbLa(Zr_{x'}, Ti_{y'}) \right] \text{ with: } y > x \text{ and } y' > x'$$

	Process 1	Process 2	Process 3	Process 4	Process 5	Process 6	Process 7	Process 8
$Q_{\%Zr > \%Ti}$	98.7%	27.7%	88.9%	45.7%	51.8%	92.7%	92.4%	64%
$Q_{\%Ti > \%Zr}$	1.3%	72.3%	11.1%	54.3%	48.2%	7.3%	7.6%	36%

Table 4

*Approximate values of (oxide reactant electronegativity) and mass.*

	mass of oxide used for each sample (g)	n (mole)	Oxide Electronegativity (ev or 1.602E-19 J) for 1mole of oxide (based on Pauling scale)	$(E_{ox})$ (ev or 1.602E-19 J) (Oxide Electronegativity*n)
<b>PbO</b>	6.5959	0.0295	2.831	0.08351
<b>TiO<sub>2</sub></b>	0.6264	0.0078	2.631	0.02052
<b>ZrO<sub>2</sub></b>	0.8828	0.0071	2.506	0.01779
<b>Sb<sub>2</sub>O<sub>3</sub></b>	1.4415	0.0049	2.796	0.01370
<b>ZnO</b>	0.4048	0.0049	2.382	0.01167
<b>La<sub>2</sub>O<sub>3</sub></b>	0.0483	0.000148	2.18	0.00032

Table 5

Absolute values of  $\Delta(E_{ox})$  (difference between oxide reactant electronegativity).

Absolute $\Delta(E_{ox})$ (ev)	PbO	TiO <sub>2</sub>	ZrO <sub>2</sub>	Sb <sub>2</sub> O <sub>3</sub>	ZnO	La <sub>2</sub> O <sub>3</sub>
PbO	-	0.06299	0.06572	0.06981	0.07184	0.08319
TiO <sub>2</sub>	0.06299	-	0.00273	0.00682	0.00885	0.01988
ZrO <sub>2</sub>	0.06572	0.00273	-	0.00409	0.00612	0.01747
Sb <sub>2</sub> O <sub>3</sub>	0.06981	0.00682	0.00409	-	0.00203	0.01338
ZnO	0.07184	0.00885	0.00612	0.00203	-	0.01135
La <sub>2</sub> O <sub>3</sub>	0.08319	0.01988	0.01747	0.01338	0.01135	-

Table 6

Evolution of attraction level (between oxide reagents) with the absolute values of  $\Delta(E_{ox})$  (difference between oxide reagents electronegativity).

Absolute values of $\Delta E_{ox}$	Attractions level	Process 1	Process 2	Process 3	Process 4	Process 5	Process 6	Process 7	Process 8
0.08319	strong attractions between oxides reagents	(PbO; TiO <sub>2</sub> )	(PbO; La <sub>2</sub> O <sub>3</sub> )	(PbO; Sb <sub>2</sub> O <sub>3</sub> )	(PbO; La <sub>2</sub> O <sub>3</sub> )	(PbO; ZrO <sub>2</sub> )	(PbO; Sb <sub>2</sub> O <sub>3</sub> )	(PbO; ZnO)	(PbO; Sb <sub>2</sub> O <sub>3</sub> )
0.07184									
0.06981									
0.06572	medium attractions between oxides reagents	(La <sub>2</sub> O <sub>3</sub> ; ZnO)	(La <sub>2</sub> O <sub>3</sub> ; ZrO <sub>2</sub> )	(La <sub>2</sub> O <sub>3</sub> ; Sb <sub>2</sub> O <sub>3</sub> )	(La <sub>2</sub> O <sub>3</sub> ; ZrO <sub>2</sub> )	(La <sub>2</sub> O <sub>3</sub> ; Sb <sub>2</sub> O <sub>3</sub> )	(La <sub>2</sub> O <sub>3</sub> ; ZnO)	(La <sub>2</sub> O <sub>3</sub> ; TiO <sub>2</sub> )	(La <sub>2</sub> O <sub>3</sub> ; TiO <sub>2</sub> )
0.06299									
0.01988									
0.01747	Low attractions between oxides reagents	(ZrO <sub>2</sub> ; Sb <sub>2</sub> O <sub>3</sub> )	(TiO <sub>2</sub> ; ZnO) – (ZrO <sub>2</sub> ; Sb <sub>2</sub> O <sub>3</sub> )	(TiO <sub>2</sub> ; ZnO)	(TiO <sub>2</sub> ; ZrO <sub>2</sub> ) – (ZnO; Sb <sub>2</sub> O <sub>3</sub> )	(TiO <sub>2</sub> ; ZnO)	(TiO <sub>2</sub> ; ZnO)	(TiO <sub>2</sub> ; ZnO)	(TiO <sub>2</sub> ; ZnO)
0.01338									
0.01135									
0.00885	Low attractions between oxides reagents	(ZrO <sub>2</sub> ; Sb <sub>2</sub> O <sub>3</sub> )	(TiO <sub>2</sub> ; ZnO) – (ZrO <sub>2</sub> ; Sb <sub>2</sub> O <sub>3</sub> )	(TiO <sub>2</sub> ; ZnO)	(TiO <sub>2</sub> ; ZrO <sub>2</sub> ) – (ZnO; Sb <sub>2</sub> O <sub>3</sub> )	(TiO <sub>2</sub> ; ZnO)	(TiO <sub>2</sub> ; ZnO)	(TiO <sub>2</sub> ; ZnO)	(TiO <sub>2</sub> ; ZnO)
0.00682									
0.00612									
0.00409									
0.00273									
0.00203									

A difference between the values of electronegativity can cause attraction or repulsion [22] between different oxides reagents, which can influence on kinetics solid reaction. Table 5 summarizes the absolute values of difference in electronegativity  $\Delta(E_{ox})$  between oxide reagents.

Therefore, based on the absolute values obtained of  $\Delta(E_{ox})$ , attractions between oxides can be classified into three categories: strong, medium and low attractions as shown in Table 6.

According to the results in Table 5, 6 and the order of reagents (oxides) addition

to the mixture for agitation, it is remarkable that there is a transfer or attraction between the entities of some oxides and others one. Arguably, (ZrO<sub>2</sub> was transferred to PbO and TiO<sub>2</sub>), (ZrO<sub>2</sub>, TiO<sub>2</sub> to PbO and Sb<sub>2</sub>O<sub>3</sub>) and (TiO<sub>2</sub> to PbO and ZrO<sub>2</sub>) for processes 1, 3 and 5 respectively. This leads to produce a maximum amount of PZT phase products. Moreover, for the processes 2 and 4, an attraction can be seen between entities of TiO<sub>2</sub>, ZrO<sub>2</sub> oxides and those of PbO and La<sub>2</sub>O<sub>3</sub> producing PLZT phase products at high rate. It has also been noticed that the choice of the mixing order between the various reactant oxides plays an important

role, because it directly affects the electronegativity difference between the oxide and consequently the attraction between them. Therefore, other oxides added to the mixture will attract the oxides that are less attracted by each other.

About the different percentage ratios obtained for (PZT / PLZT) products ( $\approx$  82.5% / 17.5%; 67% / 33%; 70% / 30%) in processes 6, 7 and 8 respectively, the results may be due to the existence of some oxides that have a greater electronegativity than others, which probably caused a spatial barrier preventing reaction between the reagents involved.

These results suggest that the selectivity in the solid-state reaction may be related to the electronegativity and the different attraction forces between reactants. Therefore, the knowledge of phase formation mechanism and kinetics is essential for the optimization of the synthesis processes [23 – 26].

## 6. Conclusion

The present article describes the solid state synthesis of piezoelectric ceramic material. It was found that the mixing methods have a significant impact on conversion, and make selective synthesis process. It can be concluded that the most important factors governing this selectivity are electronegativity and interaction forces. The use of (2) and (4) processes leads to produce PLZT with higher quantities. However, the other processes (1, 3, 5, 6, 7 and 8) can produce a major amount of PZT.

An optimum mass fraction of selected product can be obtained by taking into consideration the reactant physical properties such as electronegativity, ionic potential and attraction forces.

The present article suggests estimate the products distribution in the final synthesis mixture of advanced ceramics materials by the solid state synthesis process with suitable selectivity. Developing this study would improve the industrial efficiency of the synthesis method by solid route.

## References

- [1] B. Noheda, D.E. Cox, G. Shirane, J.A. Gonzalo, L.E. Cross, S-E. Park: *Appl. Phys. Lett.* 74(14) (1999) 2059-2061.
- [2] W. Heywang, K. Lubitz, W. Wersing: *Piezoelectricity, Evolution and Future of a Technology*, Springer Berlin, Germany 2008.
- [3] D.W. Johnson: *Am. Ceram. Soc. Bull.* 60(2) (1981) 221-224.
- [4] V. Hlavacek, J.A. Puszynski: *Ind. Eng. Chem. Res.* 35(2) (1996) 349–377.
- [5] A. Kwade, "Ultrafine comminution of ceramic raw materials part 1: Fundamentals", *CFI-CERAM*, 78(10) (2001) E37-E45 .
- [6] A. Kwade, "Ultrafine comminution of ceramic raw materials - Part 2: Application", *CFI-CERAM*, 78(11-12) (2001) E39-E44.
- [7] L.B. Kong, Y.Z. Huang, W.X. Que, T.S. Zhang, S. Li, J. Zhang, Z.L. Dong, D.Y. Tang: *Transparent Ceramics, Topics in Mining: Metallurgy and Materials Engineering*, 1st edition, Springer International Publishing, Switzerland 2015.
- [8] A. Eskandari, M. Aminzare, Z.R. Hesabi, S.H. Aboutalebi, S.K. Sadrnezhad: *Ceram. Int.* 38(4) (2012) 2627-2632.
- [9] S.H. Yu: *J. Ceram. Soc. Jpn.* 109 (2001) 65-75.
- [10] R. Roy: *Ceram. Trans.: Am. Ceram. Soc.* 95 (1998) 3-36.
- [11] L.B. Kong, J. Ma, H. Huang: *Mater. Lett.* 56(3) (2002) 344-348.
- [12] L.B. Kong, J. Ma, H. Huang: *Mater. Lett.* 56(3) (2002) 238–243.
- [13] W.J. Dawson: *Am. Ceram. Soc. Bull.* 67(10) (1988) 1673-1678.
- [14] P. Cousin, R.A. Ross: *Mater. Sci. & Eng. A*130 (1990) 119-125.
- [15] A. Sakri , A. Boutarfaia: *Materials Sciences and Applications* 4(8) (2013) 478-482.
- [16] S. Adel, B. Ahmed: *Mater. Eng. – Mater. Inz.* 21(2) (2014) 42-45.
- [17] E.M. Lifshitz: *J. Soviet Physics* 2(1) (1956) 73-83.
- [18] A. Neiman, E. Tsipis , I. Beketov , Yu. Kotov , A. Murzakaiev , O. Samatov: *Solid State Ionics* 177 (2006) 403- 410.
- [19] P.S. Bagusa, C.J. Nelinb: *Journal of Electron Spectroscopy and Related Phenomena* 194

- (2014) 37-44.
- [20] J.G. Reynolds: A revised method for estimating oxide basicity per the smith scale, with example application to glass durability: Washington River Protection Solutions, (2011). Available on: <http://www.osti.gov/scitech/servlets/purl/1028210>.
- [21] J. Portier, P. Poizot, I. M. Tarascon, G. Campet, M. A. Subramanian: *Solid State Science* 5(5) (2003) 695.
- [22] H.Wang, H. Zhong, L. Ouyang, J. Liu, D. Sun, Q. Zhang, M. Zhu: *The Journal of Physical Chemistry C* 118(23) (2014) 12087-12096.
- [23] P.K. Roy, J. Bera: *Mater. Res. Bull.* 40 (2005) 599-604.
- [24] J. Berra, S.K. Rout: *Mater. Res. Bull.* 40 (2005) 1187-1193.
- [25] A.G. Belous, O.V. Ovchar: *J. Mater. Res.* 16(8) (2001) 2350-2356.
- [26] Q. Shu, J. Zhang, B. Yan, J. Liu: *Materials Research Bulletin* 44(3) (2009) 649-653.



# MAGNETIC NANOSTRUCTURES FORMATION VIA LOCAL ANODIC OXIDATION AND MAGNETRON SPUTTERING THROUGH LITHOGRAPHIC MASK

Lenka Pravidová<sup>1,\*</sup>, Milan Vůjtek<sup>1</sup>, Roman Kubínek<sup>1</sup>

<sup>1</sup> Department of experimental physics, Faculty of Science Palacky University of Olomouc, 17. listopadu 12, 771 46 Olomouc, Czech Republic

\*corresponding author: e-mail: [pravdova.lenka@gmail.com](mailto:pravdova.lenka@gmail.com)

## Resume

Changes of magnetic properties of thin metallic films caused by the magnetron sputtering technique and by oxidation lithography were studied. The magnetic nanostructure formation was done via a lithography by sputtering the material through a mask. The anodic oxidation lithography (LAO) via scanning probe microscopy (SPM) device Ntegra Aura was used to attempt to create the magnetic nanostructures. At the beginning, the work has been scoped to the preparation and testing multilayered magnetic nanostructures based on different combinations in material composition of layers. The magnetic properties of these samples were examined by Kerr phenomenon. We observed increasing of the magnetic hardness of the magnetic nanostructure when the copper layer in the composition of ferromagnetic and antiferromagnetic multilayers has been replaced by an aluminium layer. Adding the aluminium layer onto the copper layer resulted in a decrease of magnetic hardness. This work was followed by creating of horizontal nanostructures by LAO. Changes induced by the LAO observed in the magnetic properties of the samples correspond mainly to topographical changes of the surface. Changes in the magnetic properties induced by LAO or by a variability of sputtered layers could lead to the further production of magnetic printed circuit or photonic nanostructures.

## Article info

### Article history:

Received 26 July 2016

Accepted 29 August 2016

Online 22 October 2016

### Keywords:

Local anodic oxidation;

Lithography;

Atomic force microscopy;

Magnetron sputtering;

Kerr phenomenon.

Available online: <http://fstroj.uniza.sk/journal-mi/PDF/2016/15-2016.pdf>

ISSN 1335-0803 (print version)

ISSN 1338-6174 (online version)

## 1. Introduction

Investigating the nanomaterial properties and new directions of using the acquired knowledge is driving the nanotechnology through time. Multilayers consisting of magnetic and non-magnetic metals were studied since the 90s of the last century. Combination of thin magnetic layers interlaced with thin non-magnetic layers leads to the giant magnetoresistance effect (GMR) commonly used in industry as integrated GMR sensors, such as magnetometers, differential sensors or magnetic field direction sensors (angle GMR), e.g. magnetic sensor for automotive applications [2]. Nowadays GMR elements

production consists mainly of a vacuum materials deposition on a silicon substrate and subsequent modification of the area by thermal annealing and magnetic annealing. Using photolithography, the surface is adapted so that the sensor has the greatest resistance and for its measurement small current is sufficient. Resistors of 10 k $\Omega$  were already formed as 2  $\mu\text{m}$  serpentine traces covering an area less than 100  $\mu\text{m}$  square [3]. Resistor areas are then involved in the Wheatstone bridge, where a change of the magnetic field is converted to an electrical voltage. Magnetic thin films are generally formed of iron, cobalt, nickel, or their alloys. Non-magnetic thin films are for example

copper, or chrome. But the highest GMR effect can be achieved for the combination of cobalt and copper prepared at the room temperature. As the temperature rises during the preparation of the copper and cobalt multilayers, the GMR effect decreases due to the mixing of these two materials [4]. Thanks to their magnetic performances, the materials such as cobalt and copper also have a potential use in magneto-optics, especially in the construction of photonic crystals [5 – 8]. Reaching the dimensional limits of formation of nanostructures based on the magnetic thin films is what connects GMR electronics and photonic crystals.

In our work we present possibilities for creating structured surfaces, whether applying a metallic material by magnetron sputtering through a mask, or a combination of planar sputtered sample with subsequent surface modification by applications of local anodic oxidation (LAO). The LAO is enabled by applying a bias voltage between the sample and the atomic force microscopy (AFM) probe that allows to create structures with a width of several tens of nanometers [9, 10].

## 2. Methodology

Lithographic methods can be divided into two main groups. Top-down methods [11] (material removal layer after layer to achieve the desired structure) and bottom-up methods [11] (material layering, self-organization, etc.). In our study, we focused on two bottom-up methods of transferring a structure on a substrate. They have both a common basis in the magnetron sputtering allowing thin layers deposition from units to hundreds of nanometers under a reduced pressure. In case of the first method, the smallest size of the lithographic mask structures for which this structure is transferred on a substrate at the desired topographical layout by sputtering metal materials was investigated. In case of the other method, the combination of materials and suitable setting of an oxidation lithography was investigated

for result into observable change of the magnetic properties of the substrate caused by the oxidation lithography.

### 2.1 Selection of the materials for magnetron sputtering

The selected materials - cobalt and copper - are typically used in a combination of layers for GMR reading heads of hard disks drives [1]. The principle of GMR is a reduced possibility of an electron to pass through a conductive material. Electron with spin oriented identically with magnetic domains can pass through unlike the electron with the opposite spin, which is reduced. For an antiferromagnetic configuration of the magnetic domains in the cobalt layers the resistivity is higher than for a ferromagnetic arrangement. The ferromagnetic or antiferromagnetic orientation of the individual magnetic layers of the composite material depends on the thickness of the non-magnetic interlayer as well as the rate of the magnetoresistance [4]. The GMR effect increase can be achieved by increasing the number of pairs of layers Co/Cu, adding buffer layers of Fe, or adding Al as interlayer [1]. Therefore we prepared a variation of multilayers Si/Fe/Co/[CuCo]<sub>5</sub>/Fe, Si/Fe/Co/[CuCo]<sub>2</sub>/Al/[CuCo]<sub>3</sub>/Fe, Si/Fe/Co/[CuCo]<sub>2</sub>/Al/Co/[CuCo]<sub>2</sub>/Fe and Si/Fe/Co/[CuCo]<sub>2</sub>/Al/[CuCo]<sub>2</sub>/Fe, where the Cu/Co interlayers thickness was chosen with respect to the antiferromagnetic ordering of the magnetic cobalt domains, as stated Parkin [4].

### 2.2 The oxidation rate analysis of the selected materials

Both nanostructure creation methods require sputtering various materials and therefore it is necessary to swap the sputtering targets within a single procedure. Each material target change, however, leads to sample chamber opening and exposing the already sputtered material to the influence of the ambient (oxidizing) environment. A native

oxide layer forms on each material and the composite material thus becomes poorly definable. The following Table 1 indicates the tendency of our chosen materials to react with oxygen. Oxides listed in Table 1 are the most common types formed by oxidation at room temperature. The column "E" refers to the energy that must be supplied to the system, to allow spontaneous oxidation. If the oxidation energy is positive, the material is stable. In the case of negative energy the spontaneous oxidation takes place. The more negative the value of this energy, the faster the material should oxidize. However the practical measurements as described in [12 – 14] show that the oxidation process is more complex, and for some materials the assumed oxidation rate does not correspond with actual measured values (Table 1, column "P"). The oxidation rate values for aluminum [12], iron and copper [13] and the cobalt [14] are related to the ambient temperature and normal levels of the relative humidity, i.e. 30 % - 50 %.

Table 1

*Used materials and their oxides. The column "E" gives the theoretical value of the energy needed for the oxidation of the material, the column "P" gives the values of the oxidation rate for the relative humidity in the range 30 % - 50 %.*

Material	Oxide	E (kJ.mol <sup>-1</sup> oxygen)	P (nm/30 s)
Al	Al <sub>2</sub> O <sub>3</sub>	-1045	0.6
Fe	Fe <sub>3</sub> O <sub>4</sub>	-508	2.0
Co	Co(OH) <sub>2</sub>	-422	0.8
Cu	CuO	-254	1.0

The relative humidity has the most significant effect on the course of oxidation. Below 60% of the relative humidity the oxidation progress is moderately strong and only the first few nanometers of the material oxidize. The thickness of the native oxide layer is stable after about the first minute of the exposure to the material oxidizing influence and further increases slightly. This layer forms a sort of barrier between the pure material and oxidizing environment.

For the relative humidity values between 60 % and 70 %, or by increasing the ambient temperature, the aggressiveness of the environment increases and the resistivity of the material decreases so that the oxidation takes place more easily. The progress of the oxidation rate has a logarithmic course, when after the first minute of the material exposure only a slight growth of oxide layer occurs [12].

### 2.3 Magnetron sputtering

The principle of the magnetron sputtering lies in a bombardment of a solid material target by energetic particles (ions of an inert gas), thereby the material from the target is released and deposited on the substrate. The entire process takes place under a reduced pressure. The process gas (argon) is introduced into the chamber, where in the front of the material target a glow discharge is initiated by applying a voltage. The sputtering is suitable for a deposition of conductive material layers, which can thus be prepared more effectively in a comparison with chemical processes. The quality of a deposited layer is affected, besides the material target purity, by the biased voltage and by the rotation speed of the substrate table [15].

### 2.4 Formation of nanostructures using scanning probe microscopy

The process of an intentional deformation of the surface of the sample is known as lithography and can be realized either by a mechanical or an electrochemical force. The mechanical force lithography in our case was used only as a tool for a division of the sample into smaller segments, on which an electric (chemical) lithography – the local anodic oxidation (LAO) was implemented. For the LAO the only requirement for the environment is a high relative humidity in the nearest area of the sample. The entire system must be closed in order to control the degree of the relative humidity.

In the environment with the high relative humidity a mechanical contact of submicron areas leads to spontaneous formation of a water meniscus between the tip and the sample. The meniscus is a source of oxyanions necessary for the oxidation of the sample surface. The oxidation is initiated by applying a voltage "U" to the tip [16]. The size of oxidation traces is primarily affected by the sharpness of used tip, but also by other parameters, for example by the value of bias voltage, the time for which the bias voltage is applied and by the inclination of the material to oxidize. The height of the trace and its continuity is indirectly dependent on the rate of a shift of the tip during the process.

### 3. Material and experimental methods

The used materials were prepared from material targets supplied by Quorum Technologies, namely: TK8900 Cobalt (Co) 0.3 mm thick; TK8897 Iron (Fe) 0.1 mm thick; TK8875 Aluminium (Al) 1 mm thick; SC502-314H Copper (Cu) 0.1 mm thick.

The multilayered films were sputtered on laboratory glass slides Thermo Scientific – Menzel-Gläser, extra-white soda-lime glass.

The slide glass was treated in an ultrasonic bath: firstly in a detergent and then washed in distilled water, followed by an ultrasonic bath in acetone and methanol, both for 10 minutes. The slides were dried by compressed nitrogen and for the case of the direct sputtering were put into the deposition chamber of the coating machine Q150T ES located at laboratories of the Palacky University in Olomouc. The vacuum chamber was filled with argon at the operating pressure range between  $5 \times 10^{-3}$  and  $5 \times 10^{-1}$  Pa. When combining multiple materials per sample it was always necessary to open the chamber and swap the targets. The target change time was minimized to 30 seconds. During this time the top 2 nm of iron oxidize. For cobalt and copper it was about 0.8 - 1 nm in this time period (see Table 1). During the sputtering process the layer thickness was taken into account so the sputtering/operating current was set to 25 mA for sputtering copper, 30 mA for cobalt and 50 mA for iron and aluminium. The layer deposition was carried out according to the Table. 2. Columns I - V indicates the layers of a material differing from each other in combination, and thus magnetic properties.

Table 2

The composition of the tested multilayered films is shown in columns I, II, III, mask IV and mask V. In each row there is the layer number, chosen material and layer thickness. The layers are numbered starting from the silicon substrate. The absence of a layer in the composition is marked with a "-".

Layer no.	Material	I (nm)	II (nm)	III (nm)	Mask IV (nm)	Mask V (nm)
1	Fe	5.0	5.0	5.0	5.0	5.0
2	Co	1.2	1.2	1.2	1.2	1.2
3	Cu	2.0	2.0	2.0	2.1	2.0
4	Co	1.1	1.1	1.1	1.1	1.1
5	Cu	2.0	2.0	2.0	1.2	2.0
6	Co	1.1	1.1	1.1	1.1	1.1
7	Al	-	5.6	5.6	-	-
8	Cu	2.0	2.0	-	2.1	2.0
9	Co	1.2	1.2	1.2	1.1	1.1
10	Cu	2.0	2.0	2.0	2.0	2.0
11	Co	1.1	1.1	1.1	1.0	1.1
12	Cu	2.0	2.0	2.0	2.0	2.0
13	Co	1.1	1.1	1.1	1.0	1.1
14	Fe	5.0	5.0	5.0	20	5.0
Sum (nm)	-	26.8	32.4	30.4	40.9	26.7

### 3.1 Creating structures using a mask

The combination of layers in Table 2 labeled as "mask IV" and "mask V" were directly sputtered on the substrate through a mask. As a mask the copper grid below the samples for TEM was used, namely G200 Gilder Grids, 200 mesh and Quantifoil R 3,5/1 Cu-200QC3/1, Cu grid, 200 mesh with an additional membrane 5 mesh. After the detergent, the alcohol and the nitrogen treatment the mask was fixed on the glass slides so that the surface adheres well to the treated substrate. The substrate prepared this way was placed in a chamber of the coating machine and the process of sputtering a material according to the conditions above and in the order of that in Table 1 columns "mask IV" and "mask V" started. The mask was stripped off after sputtering and the sample was ready to characterize.

### 3.2 Lithography by local anodic oxidation

The lithography by local anodic oxidation was performed using the scanning probe microscope Ntegra Aura in the contact mode of the atomic force microscopy, in the vector mode of oxidation lithography respectively, using the probe DCP20 supplied by the NT-MDT company. The oxidation was carried out for a different time duration from 500 ms to 2000 ms and for a different applied voltage from -2 V to -8 V at an artificially increased relative humidity in the range 65 – 78 %. For the purposes of the local anodic oxidation simple combinations of materials were layered. A bilayer of 20 nm Fe/ 5 nm Co was deposited on the glass slide, where cobalt forms a layer mitigating the environmental oxidizing influences so that the Fe layer is protected and therefore capable of the controlled oxidization. On the multi-layer material 5 nm Co/ 5 nm Fe/ 5 nm Co a change of the magnetic response caused by the oxidation lithography was measured. For a magnetic measurements by the magnetic force microscopy a probe NSG01/Co was used.

## 4. Results

Changes in the magnetic response caused by a change in the composition of the sample layers were shown by a measurement of the hysteresis loop using the Kerr phenomenon. The scanning electron microscope (SEM) VEGA 3 LMU by Tescan company and the scanning probe microscope Ntegra Aura by the NT-MDT company in the mode of atomic force microscopy (AFM) were used to characterize the morphological and topographic properties of the prepared samples. The characterization of the magnetic properties of the samples was performed by a magnetic gradient measurement using the magnetic force microscopy (MFM) in the dual scanning mode where the topography of the sample is measured by a semi contact AFM. The information about magnetic force sensed between the probe and the sample is collected by rescanning the already measured line of the topography of the sample using the phase shift or the frequency of the tip in a certain predetermined height above the sample surface.

The normalized magnetization of the composite material - sample I on an external magnetic field is shown in Fig. 1. The step on the hysteresis curve originates from different coercivities of cobalt and iron and is observable only for a specific angle of the sample toward the applied magnetic field.

The magneto optical response of samples I, II and III measured for the same applied magnetic field is shown in Fig. 2. Inserting the aluminum layer, respectively aluminum oxide into the composition leads to a noticeable decreasing of the coercive field and a remarkable shift of the hysteresis curve towards the positive pole of the external magnetic field. The hysteresis loop of the sample III compared to that of the sample I, however, shows an increase of the coercive field, which is caused by replacing a thin layer of copper by a twice as thick layer of aluminium, aluminium oxide respectively.

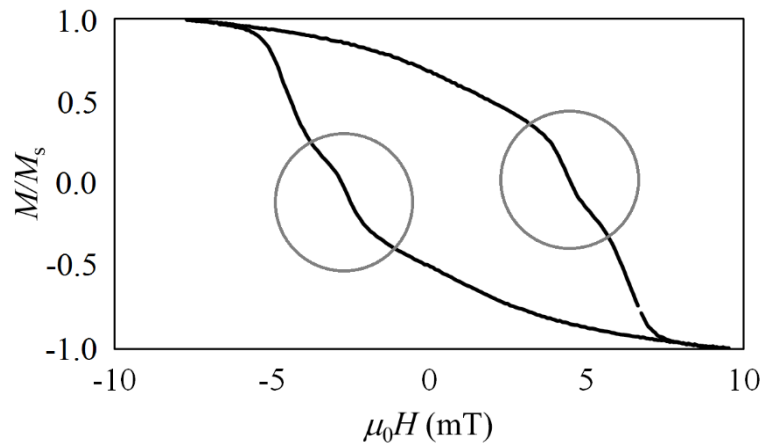


Fig. 1. The sample I - Fe/[Co/Cu]5/Co/Fe: the hysteresis curve of magnetization on external magnetic field, where  $M$  is the total magnetization of the sample and  $M_s$  is the saturation magnetization. A step marked by the grey circle has an origin in different coercivities of the cobalt and iron.

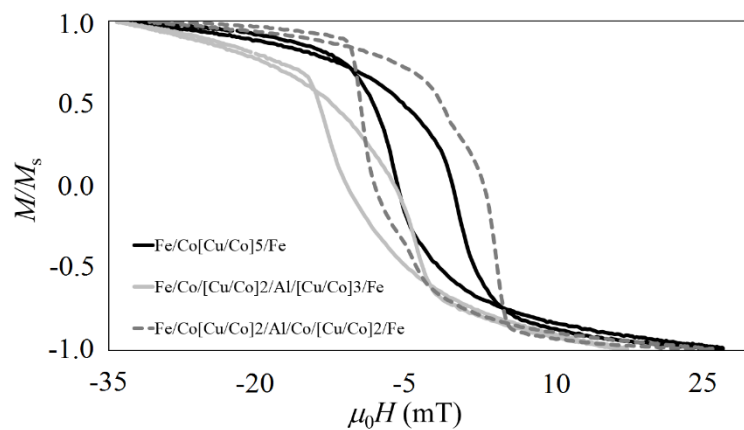


Fig. 2. The samples I, II and III: Hysteresis loops of the Kerr effect for samples I - Fe/[Co/Cu]5/Co/Fe (black), II - Fe/Co/[Cu/Co]2/Al/[Cu/Co]3/Fe (solid grey) and III - Fe/Co/[Cu/Co]2/Al/Co/[Cu/Co]2/Fe (dashed grey).

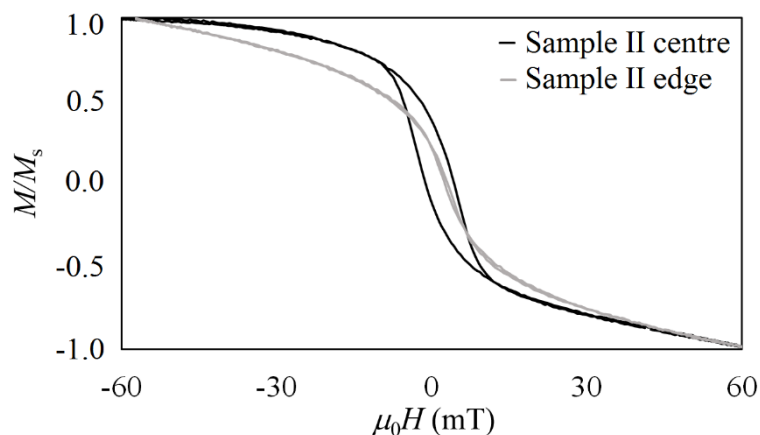


Fig. 3. The homogeneity characterization of the sputtering process on the sample II - Fe/Co/[Cu/Co]2/Al/Co/[Cu/Co]2/Fe: the black curve characterizes the detection point of the sample closer to the center of the sputtering sample holder, the grey curve characterizes the same sample but the detection point of the sample was located at the edges of the sputtering stage.

In Fig. 3 two hysteresis curves are plotted, both for the sample II. The difference between these two curves has an origin in an unbalanced sputtering process - the values of the thicknesses of the individual layers for the gray curve are smaller and the layers are likely to be inhomogeneous.

After the characterization of the surface magnetic properties, the next phase of the research took place. The material composition of the sample I has been sputtered through a lithographic mask as described above.

In the left hand side of the Fig. 4 the sputtered multilayer "mask IV" through a mask G200 is shown. The dimensions of the structure measured by the SEM and in parentheses dimensions of the masks provided by a supplier are as follows: Pitch  $120\ \mu\text{m}$  ( $125\ \mu\text{m}$ ), Hole width  $92\ \mu\text{m}$  ( $90\ \mu\text{m}$ ), Bar width  $34\ \mu\text{m}$  ( $35\ \mu\text{m}$ ). From the image and measurement it is obvious that the sputtered structure does not have a good integrity - the region collapsed. The sample "mask IV" sputtered through a mask Quantifoil R 3.5 / 1 is shown in Fig. 4 on the right. During the SEM measurements some Quantifoil membrane fragments were observed which means the membrane collapsed during the sputtering process.

From the atomic force microscopy measurement (Fig. 5) on the left the height difference of a sputtered square structure and the area covered by the mask was determined as  $40\ \text{nm}$ , which corresponds to the sum

of amount of the material sputtered in the individual layers according to Table 2. column "mask IV" ( $40.9\ \text{nm}$ ). The height of the spherical structure of the sample on the right varies from  $2$  to  $4\ \text{nm}$  instead of the expected  $26.7\ \text{nm}$ , from which we conclude that the collapse of the membrane of the masks occurred soon after the start of the sputtering.

The AFM measurement image of LAO performed on the  $20\ \text{nm}$  thick iron layer with a  $5\ \text{nm}$  cobalt cover is shown in Fig. 6. The oxidation was performed for different applied voltages (columns) and for various time exposures of the voltage at one point of the curve (lines). Although the oxidation trace for the lowest applied voltage setting and the shortest oxidation time is apparent, in case of the largest negative voltage setting applied for the longest time the oxidation did not take place. Same for some medium voltages and times. The height of an oxidation trace within one single structure ranges from a few nanometers to several tens of nanometers (e.g. for a circle oxidized at voltage of  $-8\ \text{V}$  and time of  $1000\ \text{ms}$  the height of the trace ranged from  $3.05$  to  $70.8\ \text{nm}$ ).

Fig. 7 shows a topographic measurements of the substrate  $5\ \text{nm Co}/5\ \text{nm Fe}/5\ \text{nm Co}$  with an area of an oxidized surface (top left) and the cross 68<sup>th</sup> line (top right). The MFM image and the cross-section of the same line is shown on the bottom of the Fig. 7.

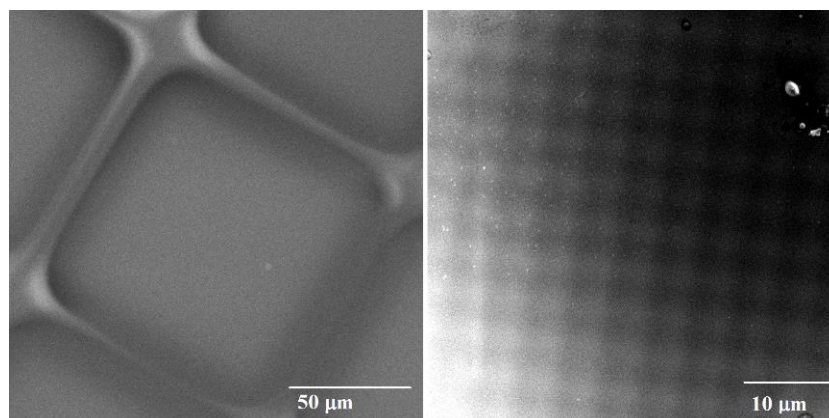


Fig. 4. The SEM snapshot of sputtering a structure through a mask G200 (left - "mask IV") and through a mask Quantifoil R 3.5 / 1 (right - "mask V").

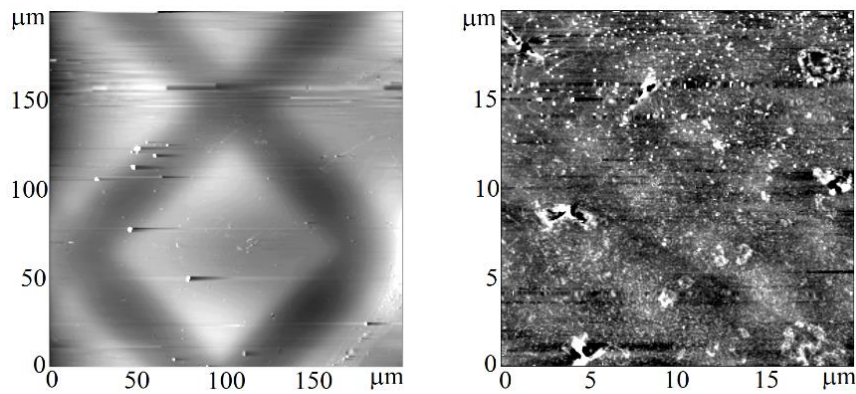


Fig. 5. The AFM image of structures sputtered through a mask G200 (left - "mask IV") and Quantifoil R 3.5 / 1 (right - "mask V").

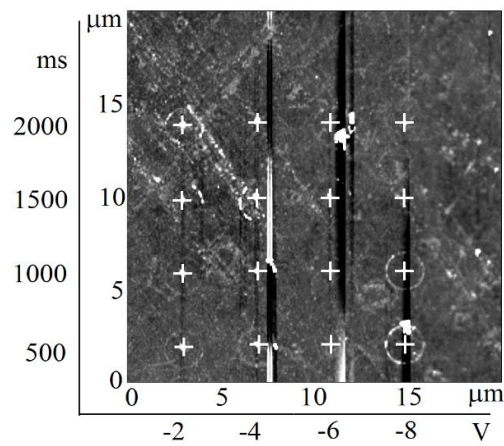


Fig. 6. The result of the LAO on 20 nm Fe / 5 nm Co: circular structures in columns were oxidized at voltages of -2 V, -4 V, -6 V, -8 V from left, for the lines oxidizing time was 500 ms, 1000 ms, 1500 ms a 2000 ms from bottom. The centre of every circular structure lithography is marked with the cross.

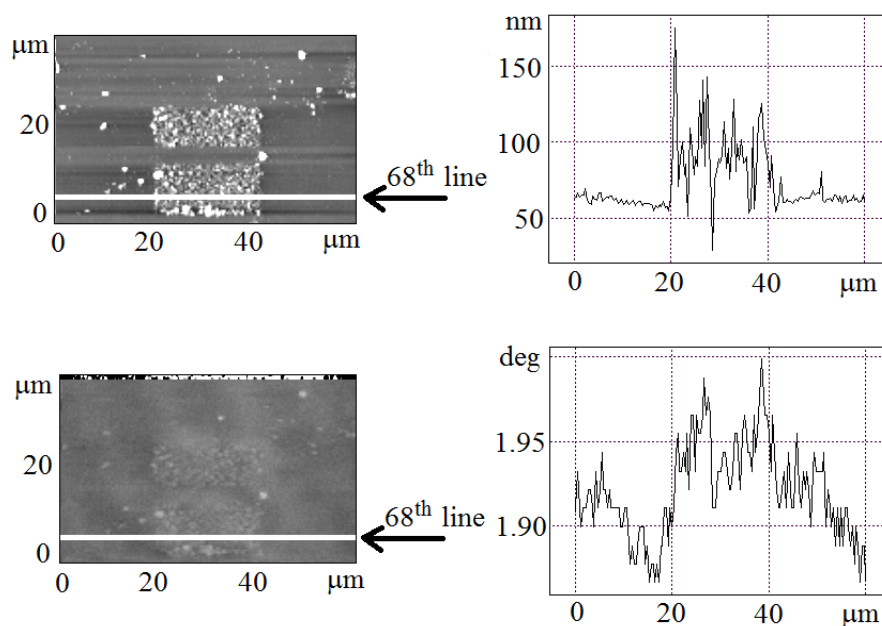


Fig. 7. The AFM LAO (upper left), and the MFM (lower left) of 5 nm Co / 5 nm Fe / 5 nm Co and the cross section and the same 68th line of the topography measurement (right).

## 5. Discussion

According to [1], the insertion of an aluminium layer into the composition of the ferromagnetic and antiferromagnetic multilayers has the effect of increasing the magnetoresistivity of the multilayer. It is shown that the substitution of one interlayer of electrically conductive copper for the aluminium (aluminium oxide respectively) leads to an increasing of the magnetic hardness of the material (Fig. 2).

Differently an addition of the aluminium oxide layer (aluminium respectively) to the copper interlayer has led to a shift of the hysteresis curve towards the positive pole of the external magnetic field (Fig. 2). That means only, a minor change of the external magnetic field is necessary for all the domains of cobalt to orient in a new direction of the magnetization. The magnetic domains in two thin adjacent layers arranges ferromagnetically or antiferromagnetically during the sputtering process. The type of the arrangement depends on the thickness of the non-magnetic interlayer [4]. Assuming the thickness of copper layers was chosen considering the antiferromagnetic arrangement, adding the aluminium layer right to an already sputtered copper layer may have resulted in the ferromagnetic ordering of the cobalt domains in the following layer, which would explain the shift of the hysteresis loop.

The homogeneity of the sputtered layers is strongly dependent on the position of the substrate within the sputtering chamber. This dependence is confirmed by the results of the measurement of the hysteresis loops for the prepared sample investigated both in the area that was closer to the center of the substrate holder during the sputtering process and the area on its edge (Fig. 3).

The result of the sputtering lithography is that the polymeric and thin membranes are unsuitable for the sputtering of thin metal layers. The sputtering process led to the collapse of the thin type Quantifoil membrane.

The reason could be in the load on the membrane produced by the sputtered material, or even in a pressure change in the chamber, which is a part of the material target replacement or in a combination of both factors. The copper grid is preferable for this technique but its disadvantage is the size of the structures that can be sputtered. The metal masks with a sufficient resolution are not easily available.

The increasing height of the oxidation traces with a rise of the oxidation time and with an increase of the applied negative voltage fit the findings on a silicon oxidation [16]. The missing oxidative traces on the lithography for this work and the large elevation changes within one oxidizing trace may correspond to an asymmetry in the sputtered cobalt coating layer, so that only in some areas the oxidation of the iron was possible.

## 6. Conclusions

The multilayered nanostructures Fe/Co/[Cu/Co]<sub>5</sub>/Fe, Fe/Co/[Cu/Co]<sub>2</sub>/Al/[Cu/Co]<sub>3</sub>/Fe, Fe/Co/[Cu/Co]<sub>2</sub>/Al/Co/[Cu/Co]<sub>2</sub>/Fe, Fe/Co and Co/Fe/Co were prepared by the magnetron sputtering method. The first results show possibilities and certain reserves of the lithographic methods same as reserves in the preparation of the samples. The used sputtering device has only one material target holder so during the material target change the already sputtered layer was exposed to the influence of the ambient (oxidizing) environment. The oxidation of the sputtered layer was minimized only by shortening the time of change of the material target, so these layers are not well material defined. Even so these multilayers are sufficient for a preliminary study of the lithographic methods.

The basic magnetic characterization of the prepared multilayers Fe/Co/[Cu/Co]<sub>5</sub>/Fe, Fe/Co/[Cu/Co]<sub>2</sub>/Al/[Cu/Co]<sub>3</sub>/Fe and Fe/Co/[Cu/Co]<sub>2</sub>/Al/Co/[Cu/Co]<sub>2</sub>/Fe was performed by their hysteresis loops measuring using the Kerr

phenomenon. Adding the aluminium layer into the composite of iron, cobalt and copper, the significant shift of the hysteresis curve was noticed. The rearrangement of the magnetic domains of the 4<sup>th</sup> cobalt layer from the antiferromagnetic to ferromagnetic arrangement towards the 3<sup>th</sup> layer can be the cause of the curve shift. Substitution of the intermediate copper layer by aluminium has led to an increase of the coercive field of the composed material without a shift of the hysteresis loop and therefore the antiferromagnetic arrangement of the individual layers of cobalt is unchanged. The measurements also confirmed the dependence of the magnetic properties of the sputtered layers on the location of the substrate in the sputtering chamber during the sputtering process.

The formation of nanostructures by sputtering the material through a mask has been successful using the grids below TEM samples. Two types of the grid were used. The lateral dimensions of the sputtered structure through the grid G200 were 125x125  $\mu\text{m}$ . The structures did not have any sharp edges. Probably while removing the mask part of the sputtered material slid off the mask. Sputtering of the structures through the secondary mask Quantifoil R 3,5/1 showed that the structures with lateral dimensions of 4  $\mu\text{m}$  are possible to prepare. However the mask itself was unsuitable due to the membrane material which collapsed after sputtering of the first 5 nm of iron.

On the prepared multilayers Fe/Co and Co/Fe/Co the local anodic oxidation was performed. The topographic deformations by the atomic force microscopy and the rate of magnetic change by the magnetic force microscopy were investigated. The topography of the oxidation trace is strongly dependent on the homogeneity and the thickness of the cover cobalt layer. According to the magnetic response measurement some magnetic changes could have been induced via the local anodic oxidation. However

the magnetic response corresponds to the topographical changes more likely.

Both multilayer preparation methods led to the formation of a structured surface. Such a structure of several square mm depending on the size of the mask can be performed by the magnetron sputtering during one single processing. The details of the structures achieve dimensions from tens to several units of  $\mu\text{m}$ . For achieving a similar result using the oxidation lithography, a macroscopic translation of the sample is needed. Combining of the individual lithographically modified areas would require a high accuracy of the translation stage. The oxidation trace itself can be even a few hundreds of nm wide which allows an incomparably better resolution of the structure than sputtering through a metal mask enables.

For an optional application of the lithography by sputtering and by oxidation for example in the field of the photonic crystals, the resolution and the material composition of the mask is necessary to solve as well as the collapse of the structure after removing the mask. One possible solution could be a combination with the method of ion beam lithography. An essential step is the use of a sputtering apparatus with more material targets so that during the sputtering process contamination of the substrate is eliminated. In the case of the local anodic oxidation the first step of improvement a change in preparation of the sample is crucial. That means to find out such configuration for which the covering cobalt material is distributed homogeneously.

### **Acknowledgements**

*This work was supported by an internal grant IGA Palacky University of Olomouc IGA\_PrF\_2014017.*

### **References**

- [1] N. Nishimura: Magnetic thin film memory element utilizing GMR effect, and recording/reproduction method using such

- memory element. U.S. Patent No 6,111,784, 2000.
- [2] C. Giebeler, D.J. Adelerhof, A.E.T. Kuiper, J.B.A. van Zon, D. Oelgeschläger, G. Schulz: *Sensors and Actuators A: Physical* 91(1-2) (2001) 16-20.
- [3] C. H. Smith; R. W. Schneider: In: *Sensors EXPO*, 1999, pp. 1-13.
- [4] S.S.P. Parkin: *Annual Reviews Material Science* 25 (1995) 357 – 88.
- [5] D.R. Lloyd; C.M. Quinn; N. V. Richardson: *Solid State Commun.* 22(11) (1977) 721-723.
- [6] I. El-Kady, M.M. Sigalas, R. Biswas, K.M.Ho, C.M. Soukolulis: *Phys. Rev. B* 62(23) (2000) 15299-15302.
- [7] S-Ch. Wu, Y.L. Yang, W.H. Huang, Y.T. Huang: *J. Appl. Phys.* 110(4) (2011) 1-6.
- [8] R. Kekesi, F. Royer, D. Jamon, M. F Blanc Mignon, E. Abou-Diwan, J. P. Chatelon, S. Neveu, E. Tombacz: *Optical Materials Express* 3(7) (2013) 935-947.
- [9] J.I. Martín et al.: *J.Magn. Magn. Mater.* 256(1-3) (2003) 449-501.
- [10] K. Watanabe, Y. Takemura, Y. Shimazu, J. Shirakashi: *Nanotechnology* 15(10) (2004) 566-569.
- [11] Ch.R.K. Marrian, D.M. Tennant: *J.Vac. Sci. Tech. A* 21(5) (2003) 207-215.
- [12] S. Shigeng, F. Placido: *Chin. Opt. Lett.* 8(1) (2010) 87-90.
- [13] S. Suzuki, Y. Ishikawa, M. Isshiki, Y. Waseda: *Mater. T. JIM* 38(11) (1997) 1004-1009.
- [14] H. G. Tompkins, J. A. Augis: *Oxidation of Metals* 16(5-6) (1981) 355-369.
- [15] P. J. Kelly; R. D. Arnell: *Vacuum* 56(3) (2000) 159-172.
- [16] L. Pravdova, M. Vujtek, R. Kubinek: In: *NANOCON 2011*, pp 384-386.



# CHARACTERISTICS OF DIAMOND – LIKE CARBON(DLC) FILM DEPOSITED BY PACVD PROCESS

Krzysztof Lukaszewicz<sup>1,\*</sup>, Agnieszka Paradecka<sup>1</sup>

<sup>1</sup>Institute of Engineering Materials and Biomaterials, Faculty of Mechanical Engineering, Silesian University of Technology, Konarskiego 18a, 44-100 Gliwice, Poland

\*corresponding author: e-mail: [krzysztof.lukaszewicz@polsl.pl](mailto:krzysztof.lukaszewicz@polsl.pl)

## Resume

Diamond – like carbon (DLC) film is promising materials for many technical and engineering applications. DLC films are used in many different industries for example: in medicine, in electronics, in optics and the automotive industry. They have excellent tribological properties (low friction coefficient), chemical inertness and high mechanical hardness.

This paper provides an analysis of the microstructure, mechanical and tribological properties of DLC films. In the study of the coating used several surface sensitive techniques and methods, i.e. High Resolution Transmission Electron Microscopy (HRTEM), Scanning Electron Microscopy (SEM), Raman spectroscopy and tribological tests like ball-on-disc.

HRTEM investigation shows an amorphous character of DLC layer. In sliding dry friction conditions the friction coefficient for the investigated elements is set in the range between 0.02-0.03. The investigated coating reveals high wear resistance. The coating demonstrated a good adhesion to the substrate.

## Article info

### Article history:

Received 28 June 2016

Accepted 11 October 2016

Online 22 October 2016

### Keywords:

Diamond – like carbon;

Tribological properties;

TEM;

Scratch test;

Ball-on-disc.

Available online: <http://fstroj.uniza.sk/journal-mi/PDF/2016/16-2016.pdf>

ISSN 1335-0803 (print version)

ISSN 1338-6174 (online version)

## 1. Introduction

Diamond-like carbon (DLC) is a metastable form of the amorphous carbon with predominance tetragonal bonds ( $sp^3$ ), characteristic of the diamond [1]. In practice, this term refers to a group of materials having both  $sp^2$  (graphite) and  $sp^3$  (diamond) bonds, but a number of  $sp^3$  bonds can vary from a few to tens of percent. The DLC coating includes both amorphous carbon (a-C) and hydrogenated carbon (a-C:H) [1, 2]. Depending on the ratio of  $sp^3$  to  $sp^2$  bonds and hydrogen content, DLC coatings are divided into several groups. The coatings of DLC type are: a-C, ta-C, a-C:Me, ta-C:H, a-C:H, a-C:H:Me (Me = W, Ti, Mo, etc.), a-C:H:X (X = Si, O<sub>2</sub>, N<sub>2</sub>) [3].

A major impact on the properties of DLC coatings is their way of deposition and humidity and the type of gas [4]. Various types of DLC

coatings are different mechanical, electrical and tribological properties. Overall, DLC coatings have a high hardness, modulus of elasticity, thermal conductivity, optical transparency in the IR spectrum and electric resistance, abrasion resistance, good fracture toughness, chemical resistance, and biocompatibility [3-7].

The most important feature is the low friction coefficient ( $< 0.1$ ) and wear resistance under the dry friction. Friction coefficient of DLC coatings also depends on the hydrogen content, the working environment and coating additives [8, 9]. This is related to the phenomenon of slip that occurs in the boundary layer through a process of graphitization and oxidation. The DLC coating is a kind of solid lubricant, consisted mainly of graphite and respective metal oxides. During friction thanks to graphitization process the layer is renewable

[1]. However, as research showed graphitization is not the only factor causing the lubricating properties of DLC. The hydrogenated DLC has good lubricating properties under dry nitrogen and argon and vacuum, wherein the graphite has lost these properties [10].

It is important to control internal stresses in DLC coatings. DLC coatings have high compressive residual stresses (0.7 GPa – 5 GPa), which tends to result in plastic deformation and poor adhesion. Reducing the residual stress can be made by doping of metallic elements (Ti, Cu, W) or non – metal (O<sub>2</sub>, N<sub>2</sub>, Si). However, this causes a reduction of hardness. Compared to the monolayer, a multilayer coating maintains high useful properties while reducing the residual stress [10, 11]. Another way to reduce internal stress is surface texturing by segmentation of DLC films [12].

Because of the unique properties, deserves special attention use of low friction DLC coatings on coverage structural elements of machines and mechanical equipment. They are operating under variables tribological and corrosive conditions. The functionality of them depends largely on the structure and properties of surface layers. The coatings and thin layers are made for the protection of contact area and to counteract of material wear processes [13]. Conventional coatings used on tools are not suited to resist friction forces because they have not enough wear resistance [14].

The aim of the paper was to examine the structure, mechanical and tribological properties of DLC coatings deposited on the X40CrMoV5-1 hot work tool steel by plasma assisted chemical vapour deposition (PACVD) method.

## 2. Experimental procedures

The tests were made on samples of DLC (diamond-like carbon) coating deposited on the X40CrMoV5-1 hot work tool steel substrate. The DLC coating was produced

by PACVD process. The DLC coating was deposited using acetylene (C<sub>2</sub>H<sub>2</sub>) as precursor. The deposition conditions were following: voltage: (-500 V), chamber pressure: 2 Pa, temperature process: 220°C. To improve the adhesion of DLC coatings, a transition CrN interlayer was deposited.

Diffraction and thin film microstructure were tested with the use of the TITAN 80–300 ultrahigh resolution scanning/transmission electron microscope. The thin cross-section lamellas for transmission electron microscopy (TEM) observations were prepared by focused ion beam (FIB) technique using Quanta 200i instrument with gallium ions.

Adhesion of the coating to the substrate material was verified by the scratch test on the CSEM REVETEST device, by moving the diamond indenter along the examined specimen's surface with gradually increasing load. The tests were made using the following parameters: load range: 0–100 N, load increase rate (dL/dt): 100 N.min<sup>-1</sup>, indenter's sliding speed (dx/dt): 10 mm.min<sup>-1</sup>, acoustic emission detector's sensitivity AE: 1.

The critical load  $L_{C2}$ , causing the loss of the coating adhesion to the material, was determined on the basis of the values of the acoustic emission  $AE$  and recorded friction force  $F_t$  as well as observations of the damage developed in the scratch test on a LEICA MEF4A light microscope.

The friction coefficient and wear rate of coating were determined in the ball-on-disc test. The tests were carried out on the T-01M (ITE) device with the following parameters: sliding speed: 0.2 m·s<sup>-1</sup>; normal load: 20 N; counterpart: Al<sub>2</sub>O<sub>3</sub> of 10 mm diameter; sliding distance: 1000 m; temperature: 22°C (± 1°C); relative humidity: 30 % (± 5%).

## 3. Results and discussion

The cross-section of the investigated DLC coating is presented on Fig. 1. The coating presents a compact structure, without any

visible delamination or defects. The morphology of the fracture of investigated coating is characterized by a dense microstructure. The fractographic observations made with the electron scanning microscope allow to state that the tested coating indicates a monolayer structure. The SEM investigation indicates the occurrence of CrN interlayer between the substrate material and the DLC coating, which affects the improved adhesion. The thickness of coating is 1.5  $\mu\text{m}$ .

Subsequently, for the coating's structure characterization, the TEM and HRTEM observations were used. The images, presented on Fig. 2 were obtained from selected regions. The bright-field images (Fig. 2a) and HRTEM micrograph (Fig. 2b) show a nanocrystalline character of DLC film. However there are also areas present in the investigated layer of quasi-amorphous nature, what was confirmed by a kind of the electro diffraction investigation. The electron diffraction patterns obtained have shown the considerable broadening of diffraction rings (Fig. 2c).

The critical load values  $L_{C1}$  and  $L_{C2}$  were determined using the scratch test method with the linearly increasing load, characterizing adhesion of the investigated coatings to the steel substrate (Fig. 3). The first critical load  $L_{C1}$  corresponds to the point at which first damage is observed (Fig. 4a); the first appearance of microcracking, surface flaking outside

or inside the track without any exposure of the substrate material - the first cohesion - related failure event. The second critical load  $L_{C2}$  is the point at which complete delamination of the coatings starts; the first appearance of cracking, chipping, spallation and delamination outside or inside the track with the exposure of the substrate material - the first adhesion related failure event (Fig. 4b). The investigated coating shows relatively high values of critical load. First failure occurs at values ( $\sim 9$  N). The second critical load values  $L_{C2}$  occurs at 37 N.

To determine the tribological properties of the DLC coating, an abrasion test under dry slide friction conditions was carried out by the ball-on-disc method. Fig. 5 presents the graph of friction coefficient  $\mu$  changes obtained during wear tests in relation to counterpart with  $\text{Al}_2\text{O}_3$ . The friction curve has initial transitional state of unstabilized course, during which the friction coefficient is reduced along with the growth of sliding distance up to obtaining the stabilized state, which normally occurs after a distance of about 100 m. Under technically dry friction conditions, after the wearing-in period, the friction coefficient recorded for the associations tested is stabilized in the range 0.02-0.03. No case of complete coatings wear-through occurred because the maximum wear-in depths were below their thicknesses (Fig. 6).

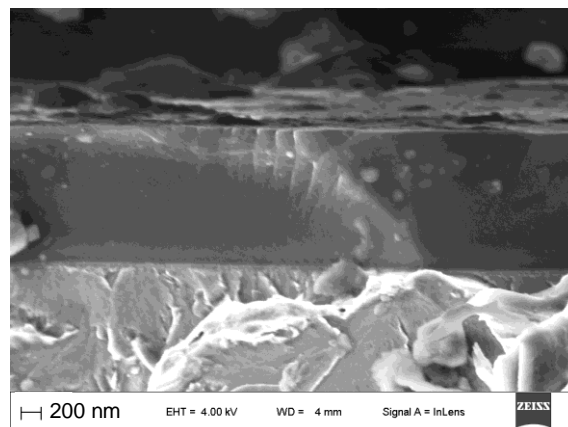
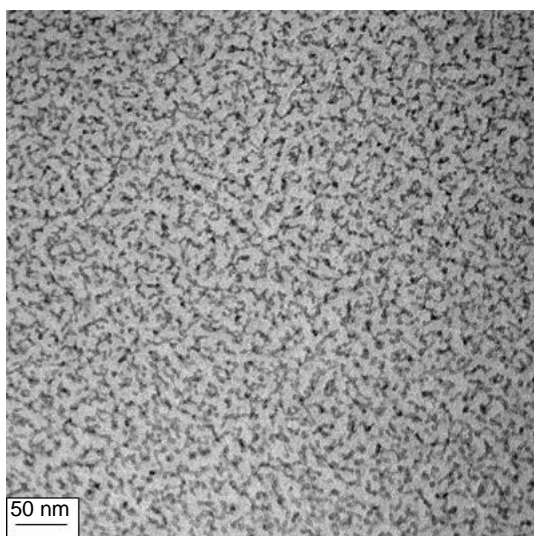
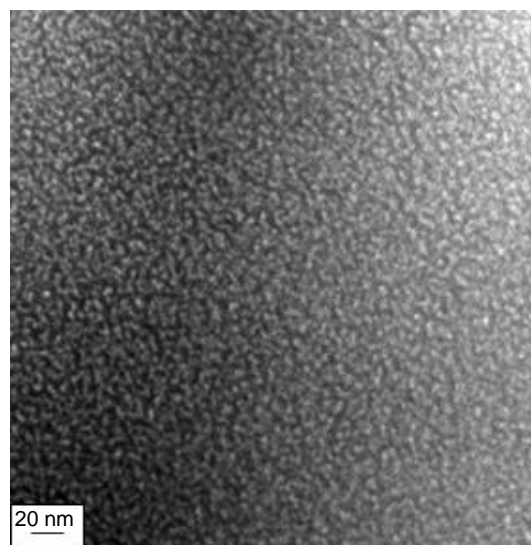


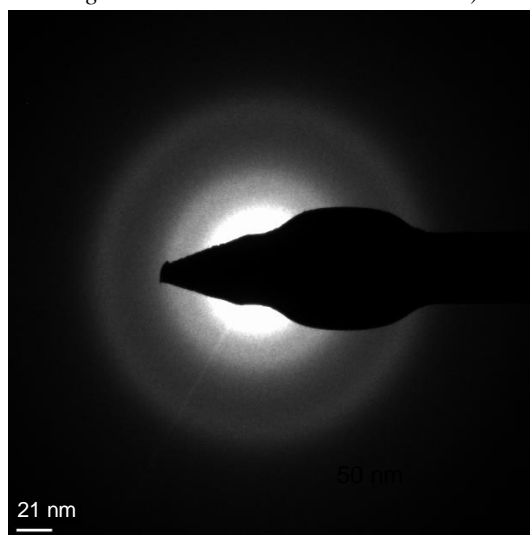
Fig. 1. SEM fracture image of DLC coating deposited onto the X40CrMoV5-1 steel substrate.



a) TEM bright-field image



b) TEM dark field image



c) corresponding SAED pattern

Fig. 2. Structure of the DLC coating.

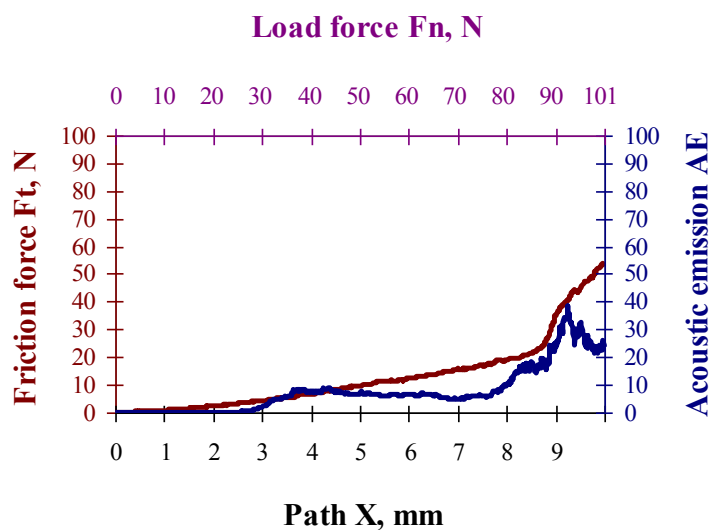
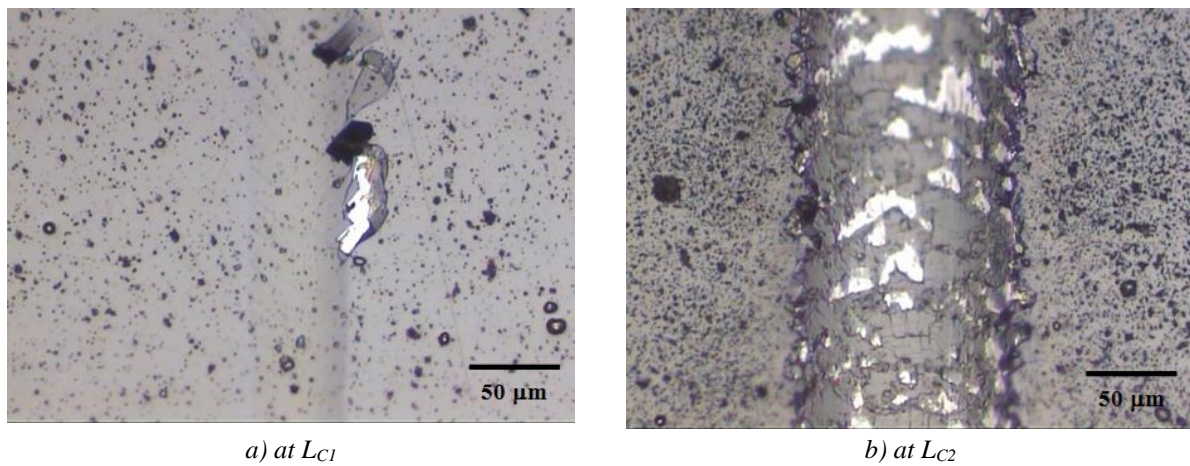


Fig. 3. Diagram of the dependence of the acoustic emission (AE) and friction force  $F_t$  on the load for the X40CrMoV5-1 steel with the DLC coating.  
(full colour version available online)



a) at  $L_{c1}$  b) at  $L_{c2}$   
 Fig. 4. Scratch failure pictures of the DLC coating on X40CrMoV5-1 steel substrate.  
 (full colour version available online)

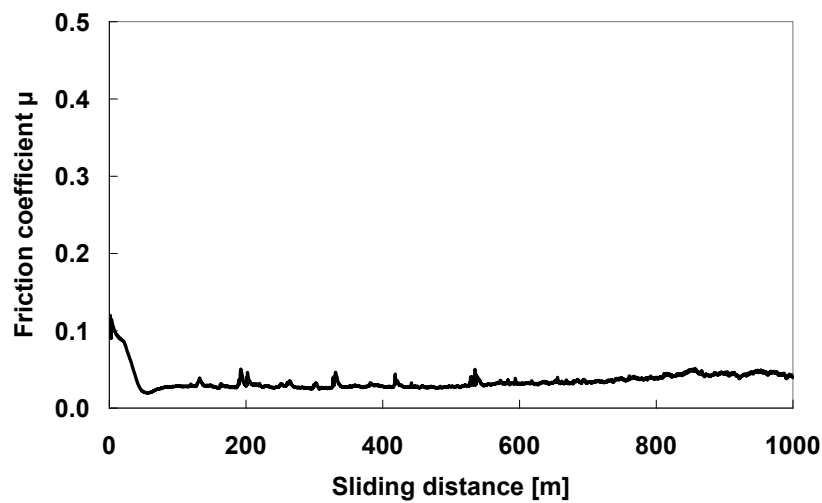


Fig. 5. Dependence of friction coefficient on sliding distance during the wear test for DLC coating.

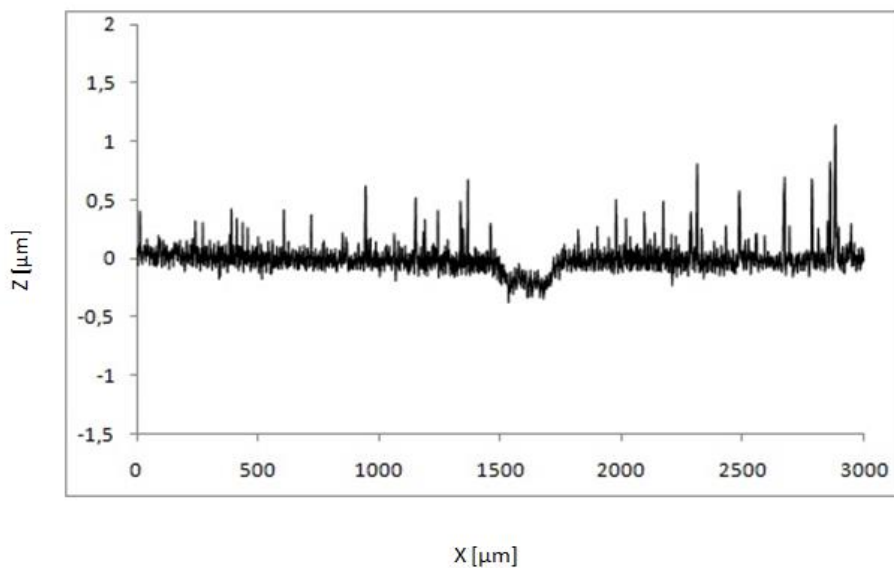


Fig. 6. Wear pattern profile after the wear test of DLC coating.

#### 4. Conclusions

Basing on the investigation results the following conclusions were arrived at:

- DLC coating was deposited successfully on X40CrMoV5-1 hot work tool steel substrate;
- the TEM investigation revealed that DLC layers have a nanocrystalline and/or quasi-amorphous structure;
- on the basis of the scratch test, it was found that the critical load  $L_{C2}$  is in the range 37 N;
- under the technically dry friction conditions, the friction coefficient is within the range 0.02-0.03.

#### References

- [1] J. Robertson: Mater. Sci. Eng. R 37(4-6) (2002) 127 – 281.
- [2] R. Crombez, J. McMinis, V. S. Veerasamy, W. Shen: Tribol. Int. 44(1) (2011) 55–62.
- [3] J. Vetter: Surface and Coatings Technology 257 (2014) 213 – 240.
- [4] M. Sedláček, B. Podgornik, J. Vižintin: Mater. Charact. 59(2) (2008) 151 – 161.
- [5] T. Bao, P.W. Morrison Jr, W.A. Woyczynski: Thin Solid Films 485 (1-2) (2005) 27 – 41.
- [6] Q. Weia, A.K. Sharma, J. Sankara, J. Narayan: Composites B: Engineering 30(7) (1999) 675 – 684.
- [7] C. Casiraghi, J. Robertson, A. C. Ferrari: Mater. Today 10 (1–2) (2007) 44–53.
- [8] S.J. Bull: Diam. Relat. Mater. 4(5-6) (1995) 827 – 836.
- [9] C. Donnet, A. Grill: Surface and Coatings Technology 94-95 (1997) 456 – 462.
- [10] Ala' A. Al-Azizi, O. Eryilmaz, A. Erdemir, S. H. Kim: Carbon 73 (2014) 403–412.
- [11] T. Takeno, T. Komiyama, H. Miki, T. Takagi, T. Aoyama: Thin Solid Films 517(17) (2009) 5010 – 5013.
- [12] T. Shimizu, T. Kakegawa, M. Yang: Proc. Eng. 81 (2014) 1884 – 1889.
- [13] S.K. Field, M. Jarratt, D.G. Teer: Tribol. Int. 37 (2004) 949–956.
- [14] M. Kalbarczyk, R. Michalczewski, W. Piekoszewski, M. Szczerek: Eksploatacja I Niezawodność 15 (2013) 319 – 324.